Supplemental S.1 Meteorological overview and mission operations

CAMP^{2}Ex operations had to conform to the spatio-temporal rhythms of the Southwest monsoon meteorology. Indeed, the Maritime Continent is an environment of extrema at timescales ranging from inter-seasonal oscillations to the mesoscale circulations of the sea breeze (e.g., Reid et al., 2012; Wang et al., 2013). In this supplemental section, we briefly place the CAMP^{2}Ex mission in meteorological context at the inter-annual and monsoonal timescales (Section S.1.1 and S.1.2, respectively), from which we briefly narrate daily airborne operations (Section S.1.3).

S.1.1 The 2019 season in perspective

There is an element of meteorological representativeness when conducting any airborne mission over a single season. Precipitation and biomass burning emissions could be unusually high or low in association with ENSO and/or the MJO/BSISO could be active or inactive, as could the associated development of tropical cyclones and monsoon enhancements (e.g., Reid et al., 2012; Wang et al., 2013). The 2019 season was an anomalous year with significant drought and burning, as well as seasonally unusual weather. Figure S.1.1 (a) provides a 2000-2021 time series of the Standardized Precipitation Evapotranspiration Index (SPEI; Begueria et al., 2013) global drought monitor using a 6 month averaging kernel over two domains: Borneo (6^o S-8^o N Latitude and 108^o-120 ^{o} E Longitude) and Sumatra + Malay Peninsula (6^o S-8^o N Latitude and 95^o-108^o E Longitude). For comparison, as a gross indicator of fire activity, also included is the Terra MODIS average 550 nm aerosol optical depth (AOD; Levy et al., 2013) over an area average domain that covers Sumatra through Borneo (6^o S-8 ^{o} N Latitude and 95^o-120 ^{o} E Longitude). A temporal zoom for the previous 5 years up to and including CAMP^{2}Ex (2015 through 2019) is provided in Figure S.1.1 (b) along with major tropical indicators of El Nino (Multivariate ENSO Index V2; Wolter and Timlin, 2011), El Nino Modoki (Ashok et al., 2007), and the Indian Ocean Dipole (IOD, Saji et al., 1999) in Figure S.1.1 (c). Clearly, the region can host strong seasonal variability in interannual to seasonal atmospheric variability, drought, and fire activity.

The drought throughout Indonesia 2019 season was associated with the third highest MODIS AOD_{550} monthly average since Terra MODIS data records began (the September 2019 average AOD_{550} of 0.82 behind only the 2006 and 2015 El Nino related fire events). While major events have occurred during every drought period regardless of season from significant agricultural burning (e.g., January 2005: Reid et al., 2012; and June 2013: Koblitz et al., 2018; Oozeer et al.,

2020) the largest events typically occur in September and October, at the end of the Southwest Monsoon (SWM) and into the early Northeast Monsoon seasons. The 2019 burning season was no different in this regard. ENSO induced drought has long been identified as the strongest forcing agent for biomass burning (e.g., Nicholes et al., 1989; Field and Shen, 2008). However, other meteorological modes are important, including the timing of MJO/BSISO propagation, El Niño Modoki and IOD (e.g., Reid et al., 2012). The ENSO MEIv2 index for the 2015 fire outbreak was the strongest since the record breaking 1997 event, being above 1 from May through July 2015 and peaking above 2 during the August through Oct 2015 peak burning. In comparison, the 2019 MEI had weak El Niño conditions, registering 0.5-0.8 for January through March. Nevertheless, based on the ERA5 reanalysis (Hersbach et al., 2020) the region spanning Sumatra through Borneo (6° S-8 ° N Latitude and 95°-120° E Longitude) showed rainfall anomalies in the April-October time period associated with summer burning were similarly down ~18% from a typical 136 cm. In comparison, the 1997 El Nino exhibited a 32% negative anomaly.

The details of the anomalous behavior of the 2019 season are outside the scope of this paper's supplemental material. However, several noteworthy characteristics are worth highlighting. First, while El Nino was neutral to weak, nevertheless, warm sea surface temperature anomalies in the central Pacific and cooler waters around the MC were present, as indicated by the El Nino Modoki event on Figure S.1.1(b). These conditions are known to bring negative precipitation anomalies to the MC (Ashok et al., 2007). Second, 2019 exhibited an early monsoon transition, on and around September 21-23, 2019 in comparison of more typical early October (Reid et al., 2012), This transition was associated with a stalled BSISO/MJO event (e.g., Section S.1.2 and Reid et al., 2012) and resulted in earlier than usual easterly winds over the Indian Ocean, and possibly contributed to a near record IOD event that formed post-CAMP^{2}Ex (e.g., IOD index in Figure S.1.1(b)).

Hydrological perturbations throughout the region in 2019have been recently studied. Lu and Ren, (2020) observed, as early as May 2019, a strong Australian High and lowering sea level pressure over the Philippines and South China Sea, which created exceptionally strong cross equatorial flow, a pattern resulting in subsidence over the MC. However, except for a wet period in Aug., 2019, the drought index indicated increasing drought starting in February. Clearly, several factors may be at play (early season El Niño, Modoki, and Australian high). Qi et al., 2021 noted the near record fall IOD event along with the stalled MJO/BSISO, brought drought to eastern China that fall. At the same time, these conditions brought drier early Indian Monsoon conditions, but wetter conditions later (e.g., Ratna et al., 2021). Lu and Ren (2020) noted the indicators of these anomalies were visible in seasonal forecasts, giving some hope to their predictability in the future.

S.1.2 The CAMP^{2}Ex Airborne Operations Period

The six-week CAMP^{2}Ex airborne intensive operations period was planned to coincide with a number of meteorological conditions. These included: a) the end of the southwest monsoon (SWM) season, when the likelihood of biomass burning in Borneo is at a maximum during periods with the possibility of Asian transport into the operations area (Reid et al., 2012; 2013); b) within a 45-day window for the intra-seasonal Madden Julian Oscillation (MJO) / Boreal Summer Intra-seasonal Oscillation (BSISO; Jian and Wang., 2004; Zhang, 2005; Reid et al., 2012); and c) with the typhoon season, to capture several major typhoon-related monsoon enhancements that can lead to strong biomass burning injections into the operations area (Reid et al., 2012; Wang et al., 2013). For reference, a temporal operations and meteorological synopsis for August through October 2019 is provided in Figure S.1.2.

The nature of convection and transport of pollutants in the operations area is indicated by daily variability in monsoon strength and tropical cyclone (TC) activity. These are depicted in Figure S.1.2(a) with the 925 hPa ERA5 meridional velocity being used as an indicator of monsoonal strength for three locations: Riau Island (4.5 N; 107.5 E) as characteristic of the southern South China Sea and Maritime Continent; West of Luzon (15.5 N; 119.5) ~1000 km to the NNE as characteristic of the northern South China Sea environment; and East of Luzon at the Sally Ride station point (16.5 N; 127.5) as characteristic of the North Tropical Western Pacific (NTWP) ~800 km west of the North Luzon point. Monsoon strength varied on roughly weekly timescales and was largely associated with the passage of the quiescence following TC activity. Markers for tropical disturbances that developed or passed west of 130 E are included in Figure S.1.2 (a). The early days of the mission experienced moderate quiescence, followed by a strong monsoon enhancement five days later due to TS Kajiki passing over Luzon, and subsequently TY Lingling developing over the northern South China Sea. A monsoonal break then occurred from Sept. 8-13, 2019, followed by a second monsoon enhancement Sept 14-19 due to a NTWP monsoon gyre that eventually evolved into TY Tapah. After Tapah left the region, the full monsoon transition occurred over the Sept 21-23 period, as evidenced by a reversal in sign in the meridional wind across all domains. The final storm to impact the mission was TY Mitag, which passed closely east of Luzon on Sept 30, 2019. While bringing strong southerly winds to the east of Luzon, Mitag was not quite strong enough to reverse winds over the South China Sea.

CAMP^{2}Ex captured portions of the BSISO/MJO across two cycles (Figure S.1.2(c) with additional markers when amplitudes were >1). The operations period also fortuitously coincided with most of the BSISO/MJO cycle from phase 3 (where an active phase of convection is entering the MC) to phase 8 (when the MC is largely in a convectively suppressed phase). Not surprisingly, as the BSISO is a boreal summer multi modal phenomenon including the MJO (Wang and Xie, 1996), the BSISO and MJO indices are well correlated, although the BSISO had turned for the season and shows statistically significant amplitude >1 throughout the IOP. The BSISO/MJO then stalled during the last week of CAMP^{2}Ex, but regained its westward propagation in late October. The BSISO/MJO indices, monsoon enhancements, and TC activity conceptually matched regional precipitation, depicted by Figure S.1.2(d), with IMERG derived precipitation for boxes containing Borneo's southern Kalimantan and Sumatra (6S-8N; 95-120E), and Luzon and a portion of the NWTP out to the Sally Ride operations area(10-20N; 117-130E). Over Indonesia, the little SWM precipitation that did occur, happened as the BSISO entered the region from the Indian Ocean later in August. Precipitation then returned in late September with the formation and propagation of the MJO into the MC-an event that very well may have been linked to the early monsoon transition. As befitting the border of the monsoon trough, the Luzon-Sally Ride region always hosted some convective activity until the monsoon transition. After the transition, precipitation was punctuated by TY Mitag, but scattered CBs were typically present over the whole region.

Biomass burning emissions from Indonesia were understandably out of phase with precipitation. Figure S.1.2(d) provides Fire Locating and Modeling of Burning Emissions (FLAMBE, Reid et al., 2009; Hyer et al., 2013) daily estimates of biomass burning Particulate Matter <2.5 μm ($PM_{2.5}$) emissions for the islands of Borneo and Sumatra. Corresponding AERONET interpolated 550nm AOD for sites with operational data during the mission are provided (site locations provided in Figure S.1.2(e) include: 1) Palangkaraya Borneo (2.2S; 113.9E)) and Jambi Sumatra (1.6S; 103.6E) in the heart of burning regions; and 2) receptor sites at Singapore(1.3N; 103.8E), Taiping Island in the South China Sea(10.4N; 114.4E), and Marbel University on Mindanao(6.5N;

124.8E)). Periods of agricultural or slash burning resulting in AODs above 0.5 to 1 are common in the region from June through August - whenever there are several days of dry weather (Reid et al., 2012). However, after Sept 1 the region dried sufficiently to support large-scale burning in the peat forests, only to tail off after the monsoon transition with the return of some precipitation. Nevertheless, drought and burning continued until late November, when the water table rose sufficiently to saturate peat fields and extinguish combustion. Atmospheric smoke loadings, as inferred from AERONET AOD, show exceptionally high aerosol loadings akin to the mammoth 2015 extreme El Nino burning event (Eck et al., 2015), with AOD values reaching over 7 on Borneo and Sumatra (99.9% direct solar beam attenuation) - a value so high that it could only be estimated through the use of the 1.6 µm channel where smoke extinction is less than a fifth of that at 550 nm. Such events are hypothesized to suppress convection and further enhance drought and burning (Tosca et al., 2010). Fifteen hundred kilometers away from the source region during the second monsoon enhancement, at Marbel, Mindanao, and Taiping Island in the South China Sea, AOD reached 1 and 2, respectively (or 63% and 86% direct beam attenuation from the earth to the surface).

S.1.3 CAMP^{2}Ex Airborne Operations

Mission operations and daily targets were dictated by variability in monsoon strength and tropical cyclone (TC) activity. Included in S.1.2 (f) are P-3, Learjet 35 flights and Sally Ride on station periods, including halos for cross-platform coordination. An associated flight calendar is provided in Table S.1.1. The P-3 operated across the entire planned Aug 25-Oct. 5, 2019 mission period without any maintenance cancellations. On only two occasions were there minor flight delays due to maintenance and instrumentation. The SPEC Learjet 35 arrived 10 days after mission initiation, and departed early on September 30th having exhausted its flight hours. The SPEC Learjet 35 also operated without any unplanned maintenance delays. The PISTON R/V Sally Ride was on station for 20 days in the middle of the campaign, on Sept 5-25th, 2019.

Flight operation areas, objectives and plans were typically decided two days in advance. Because flight data and file naming conventions are based on UTC time at takeoff (GMT +8), users should be mindful of differences between data's UTC based and "local Philippine" dates. Each flight had a particular focus area application and appropriately selected flight scientists, but each flight addressed objectives for multiple focus areas. Flight plans followed differences in the regional meteorology, and thus also tended to have regional foci. For example, flights over the Sulu Sea (local days Aug 30, 31; Sept 4, 16; e.g., Figure 1 (a)) generally focused on emissions and radiative environment of outflow from Borneo, including 2019's massive peat burning plume. Nevertheless, Aug 30 also provided sampling of land breeze convection. These flights all occurred in the first half of the mission in association with monsoon breaks or early development. Flights near Luzon (local time zone days of Aug 25, 27; Sep 9, 28, 29; Oct 4; e.g., Figure 8(a)) were conducted focusing on the aerosol environment in the vicinity of isolated and organized convection. North of Luzon, with its climatologically lower cirrus fraction, supported radiation focused flights, including sunrise flights, as well as characterization of Asian emissions (Sept 14, 20; Oct 2). Flights over the NTWP (Sep 8, 17, 19, 22, 24, 25; Oct 5) included three P-3 and five Learjet 35 flights over the Sally Ride (Sep 8, 22, 24) focused on smoke transported into mildly convective environments and clean marine air. Most of these flights occurred during the post monsoon transition owing to the more scattered nature of convection. Finally, flight components were dedicated to sampling the metro Manila super plume (e.g., Sept 14, Oct 4) along with systematic take-off and landing collections at Clark.

While the P-3 flight timeline was planned in detail two days before takeoff, the SPEC Learjet 35 was used much more tactically. Given its shorter 4 hour endurance but higher 450 knot transit speed, the SPEC Learjet 35 was placed on standby and then rapidly scrambled when appropriate convection targets were developing. Examples include characterizing convection being scanned by the Sally Ride SeaPOL radar (Sept 10, 13, 15, 17, 21), flying in tight coordination with or underneath the NASA P-3 (Sept 20; 21; 24; 25; 29), or characterizing regional convection too deep for the NASA P-3 to sample (Sept 7, 9, 17).

S.1.4 CAMP^{2}Ex Sampled Environments

As demonstrated in Figure 1 of the main body of the paper, and by this supplemental section, CAMP^{2}Ex sampled a wide variety of dynamical, thermodynamic, and composition environments. These can be loosely categorized into several dimensions: monsoon and post monsoon (delineated ~Sept 22); monsoonal surge (Sept 6-8; Sept 15-17) versus quiescence, and pristine to polluted (throughout the mission). Regarding pollution loadings, significant sources ranged from mainland Asia to the metro Manila super plume, and the aforementioned biomass burning ejection events from Borneo. Large-scale flow patterns also afforded opportunities to sample air originating from the remote NWTP. Included in Table S.1.1 are notes on each flight. Additional information on airmass histories sampled by the P-3 are provided in Hilario et al., (2021).

One of the more challenging aspects of CAMP^{2}Ex's assessment of aerosol impacts on clouds is accounting for the overall meteorological state. The Sept 6th case study discussed in the main body of this paper (Figure 7) shows the many dimensions of state that must be considered. As another example, Figure S.1.3 and S.1.4 provide additional context near the time and location of the Figure 1 data, providing AHI true color images and skew-T diagrams of relevant dropsondes. Research flights 9 and 10 (Sept 16-17, 2019 local date) demonstrated another monsoon enhancement with biomass burning transport observed from Borneo through the Philippines and into the monsoonal trough. Included in the figures are the region with the P-3 at the time of the dropsonde dispatch, and its last hour flight track, For the dropsonde off of Sabah Borneo at ~0Z Sept 16th (Figure S.1.3-upper row; Figure 1 (c)) the sounding represents what is a fairly common occurrence for polluted boundary layers -overall a dry profile with altitude ranges of adiabatic lapse rates but with multiple inversions and associated moisture levels. The mixed layer height was ~450 m and associated with a weak inversion having scattered clouds of ~ 200 m deep. Above this, warm moist inversions are often at the top of aerosol detrainment layers and associated with congestus tops and altocumulus (e.g., Reid et al., 2019). As seen in Figure 1(b) lidar profiles, biomass burning smoke was largely transported within the mixed layer and up to the 1.5 km/975 hPa inversion for ~1500 km from origin, with scattered cumulus. Likewise, aerosol layers and scattered altocumulus were found at 2200 m/800 hPa and 3 km/700 Pa inversion levels. The top most inversion at ~590 hPa/4.5 km that is in association with the well-known 0^{o}C detrainment layer of deep convection (e.g. Johnson et al. 1996, 1999; Posselt et al., 2008) also shows an isolated aerosol layer. In contrast, for the flight the next day east of Luzon, the air mass had travelled over the ocean for an additional 1200 km and the ~0Z Sept 17^{h} dropsonde (Figure S.1.3- middle row; Figure 1 (d)) shows a deeper MBL and a much more moist profile. Here, the primary smoke plume was in the MBL, with lower particle concentrations but better mixed smoke to 3 km/710 hPa, the location of the strongest inversion. Finally, four hours later the P-3 sampled the outflow of an MCS across the boundary delineating smoke and pristine conditions. This profile exhibited higher overall moisture, and isothermal layers, and perhaps subsidence inversions associated with congestus tops at 520 hPa/5500 m (Figure S.1.3 lower row; Figure 1 (e)). Ultimately this case demonstrates how the smoke and the thermodynamic environment evolve together during transport from source, and that its' final fate 3000 km downwind and must be accounted for in the analyses.

In addition to the monsoon enhancement induced smoke event referred to in the previous paragraph, CAMP^{2}Ex captured a variety of cloud type and thermodynamic environments, some of which are included in Figure 1, such as land breeze induced convection, cold pools, and fields of congestus (Figure 1 (f), (g), and (h), respectively). Figure S.1.4's upper, middle and lower panels provide the associated AHI true color imagery and thermodynamic soundings respectively. Coastal convection was commonplace, with the first research flight to the Sulu Sea (Research Flight 3, August 31st local time; Figure 1(f) and Figure S.1.4 upper panel) being able to observe a string of thunderstorms triggered in association with a land breeze propagating earlier in the morning from Palawan Island with relatively clean conditions. The profile was moderately moist with lapse rate near the moist adiabat, and the monsoon flow weak. Indeed, winds were light, even becoming NW above the MBL. Nevertheless, weak isothermal layers are present and one notable dry layer was seen at 660 hPa. Cold pools were also prevalent, with the case of Research Flight 7 (local date Sept. 9th; Figure 1 (g) Figure S.1.4 middle panels) capturing a well-defined cell and cold pool in a region of moderate shear and reduced lapse rate. Finally, there were periods of monsoonal quiescence and notably the monsoon reversal around Sept 22nd. Even with a weak or reversed monsoon, organized tropical disturbances to typhoons propagated across the region. The October 5th case typifies these environments (Figure 1 (f) and Figure S.1.4 lower panels), with a isothermal layer to nearly 800 hPa but with isolated congestus reaching 600 hPa. This case was formed by a vorticity maximum propagating from the NWTP to north of Luzon.

Supplemental S.1 References

Ashok, K., Behera, S. K., Rao, S. A., Weng, H., and Yamagata, T. (2007), El Niño Modoki and its possible teleconnection, *J. Geophys. Res.*, 112, C11007, doi:10.1029/2006JC003798.

Beguería, S., Vicente-Serrano, S.M., Reig, F. and Latorre, B. (2014), Standardized precipitation evapotranspiration index (SPEI) revisited: parameter fitting, evapotranspiration models, tools, datasets and drought monitoring. Int. J. Climatol., 34: 3001-3023. https://doi.org/10.1002/joc.3887

Eck, T. F., Holben, B. N., Giles, D. M., Slutsker, I., Sinyuk, A., Schafer, J. S., Smirnov, A., Sorokin, M., Reid, J. S., Sayer, A. M., Hsu, N. C., Shi, Y. R., Levy, R. C., Lyapustin, A., Rahman, M. A., Liew, S.-C., Salinas Cortijo, S. V., Li, T., Kalbermatter, D., Keong, K. L., Yuggotomo, M. E., Aditya, F., Mohamad, M., Mahmud, M., Chong, T. K., Lim, H.-S., Choon, Y. E., Deranadyan, G., Kusumaningtyas, S. D., Aldrian E., 2019: AERONET remotely sensed measurements and retrievals of biomass burning aerosol optical properties during the 2015 Indonesian burning season. *Journal of Geophysical Research: Atmospheres*, 124, 4722– 4740. https://doi.org/10.1029/2018JD030182

Jian, X., Li, T., Wang, B., 2004: Structures and mechanisms of the northward propagating boreal summer intraseasonal oscillation, J. of Climate, 17, 1022-1039, https://doi.org/10.1175/1520-0442(2004)017<1022:SAMOTN>2.0.CO;2

Johnson, R. H., P. E. Ciesielski, and K. A. Hart, 1996: Tropical inversions near the 0°C level, *J. Atmos. Sci.*, **53**, 1838– 1855.

Johnson, R. H., T. M. Rickenbach, S. A Rutledge, P. E. Ciesiekski, and W. H. Schubert, 1999: Trimodal characteristics of tropical convection, *J. Clim.*, **12**, 2397– 2418.

Hersbach, H., Bell, B., Berrisford., P., Hirahara, S., et al. 2020: The ERA5 global reanalysis. *Q J R Meteorol Soc*., 146, 1999– 2049. https://doi.org/10.1002/qj.3803

Koplitz, S. N., Mickley, L. J., Jacob, D. J., Marlier, M. E., DeFries, R. S., Gaveau, D. L. A., Locatelli, B., Reid, J. S., Xian, P., and Myers, S. S., 2018: Role of the Madden-Julian Oscillation in the transport of smoke from Sumatra to the Malay Peninsula during severe non-El Niño haze events. *Journal of Geophysical Research: Atmospheres*, 123, 6282– 6294. https://doi.org/10.1029/2018JD028533

Levy, R. C., Mattoo, S., Munchak, L. A., Remer, L. A., Sayer, A. M., Patadia, F., and Hsu, N. C., 2013: The Collection 6 MODIS aerosol products over land and ocean, Atmos. Meas. Tech., 6, 2989–3034, https://doi.org/10.5194/amt-6-2989-2013.

Lu, B., & Ren, H.-L. 2020: What caused the extreme Indian Ocean Dipole event in 2019?*Geophysical Research Letters*, 47, e2020GL087768. https://doi.org/10.1029/2020GL087768

Qi, L., Ji, Y., & Zhang, W. (2021). Indispensable role of the Madden-Julian oscillation in the 2019 extreme autumn drought over eastern China. *Journal of Geophysical Research: Atmospheres*, 126, e2020JD034123. https://doi.org/10.1029/2020JD034123

Oozeer, Y., Chan, A., Wang, J., Reid, J.S., Salinas, S.V., Ooi, M.C.G., Morris, K.I., 2020: The uncharacteristic occurrence of the June 2013 biomass-burning haze event in Southeast Asia: Effects of the Madden-Julian Oscillation and tropical cyclone activity. *Atmosphere* 2020, *11*, 55. https://doi.org/10.3390/atmos11010055

Posselt, D. J., van den Heever, S. C., and Stephens, G. L., 2008: Trimodal cloudiness and tropical stable layers in simulations of radiative convective equilibrium, *Geophys. Res. Lett.*, 35, L08802, doi:10.1029/2007GL033029.

Ratna, S. B., Cherchi, A., Osborn, T. J., Joshi, M., & Uppara, U., 2021: The extreme positive Indian Ocean dipole of 2019 and associated indian summer monsoon rainfall response. *Geophysical Research Letters*, 48, e2020GL091497. https://doi.org/10.1029/2020GL091497

Reid, J. S., Hyer, E. J., Johnson, R. S., Holben, B. N., Yokelson, R. J., Zhang, J., Campbell, J. R., Christopher, S. A., Di Girolamo, L., Giglio, L., Holz, R. E., Kearney, C., Miettinen, J., Reid, E. A., Turk, F. J., Wang, J., Xian, P., Zhao, G., Balasubramanian, R., Chew, B. N., Janjai, S., Lagrosas, N., Lestari, P., Lin, N. H., Mahmud, M., Nguyen, A. X., Norris, B., Oanh, N. T. K., Oo, M., Salinas, S. V., Welton, E. J., and Liew, S. C., 2013: Observing and understanding the Southeast Asian aerosol system by remote sensing: An initial review and analysis for the Seven Southeast Asian Studies (7SEAS) program, Atmos. Res., 122, 403–468, doi:10.1016/j.atmosres.2012.06.005.

Reid, J. S., Xian, P., Hyer, E. J., Flatau, M. K., Ramirez, E. M., Turk, F. J., Sampson, C. R., Zhang, C., Fukada, E. M., and Maloney, E. D., 2012: Multi-scale meteorological conceptual analysis of observed active fire hotspot activity and smoke optical depth in the Maritime Continent, Atmos. Chem. Phys., 12, 2117–2147, doi:10.5194/acp-12-2117-2012.

Saji, N. H., B. N. Goswami, P. N. Vinayachandran, and T. Yamagata, 1999: A dipole mode in the tropical Indian Ocean. Nature, 401, 360-363. https://doi.org/10.1038/43854

Tosca, M. G., Randerson, J. T., Zender, C. S., . Flanner, M. G., Rasch, P. J., 2010: and Do biomass burning aerosols intensify drought in equatorial Asia during El Niño?, Atmos. Chem. Phys., 10, 3515–3528, https://doi.org/10.5194/acp-10-3515-2010.

Wang, J., Gei, C., Yang, Z., Hyer, E. J., Reid, J. S., Chew, B. N., and Mahmud, M. 2013: Mesoscale modeling of smoke transport over the Southeast Asian Maritime Continent: interplay of sea breeze, trade wind, typhoon, and topography, *Atmos. Res.*, 122, 486-503, https://doi.org/10.1016/j.atmosres.2012.05.009.

Wang, B., and Xie, X. (1997). A Model for the Boreal Summer Intraseasonal Oscillation, Journal of the Atmospheric Sciences, 54(1), 72-86. Doi: https://doi.org/10.1175/1520-0469(1997)054%3C0072:AMFTBS%3E2.0.CO;2

Wolter, K., and M. S. Timlin, 2011: El Niño/Southern Oscillation behaviour since 1871 as diagnosed in an extended multivariate ENSO index (MEI.ext). *Intl. J. Climatology*, 31, 14pp., 1074-1087. DOI: 10.1002/joc.2336.

Zhang, C., M., 2005: The Madden-Julian Oscillation, Rev. Geophys., 43, RG2003, doi:10.1029/2004RG000158

Table S.1.1 CAMP^{2}Ex Flight Calendar. Provided are: the local date of operations (Philippine Standard Time); the P-3 flight number and takeoff time in UTC used in CAMP^{2}Ex data files; Learjet flight number and takeoff time; region of operations; a description of the target or any other notes. Superscripts are provided on flight numbers to indicate coordinated flights: ^{r} Regional coordination between P-3 and Learjet 35; * Tight coordination between P-3 and Learjet 35; $^{\#}$Aircraft sampling in Sally Ride SEAPOL radar range. Other abbreviations include: MBL-Marine Boundary Layer; Ac-altocumulus clouds; CB-thunderstorm; TCCON-Total Carbon Column Observing Network

Local Date	P-3 #: Takeoff (UTC)	Learjet #: Takeoff	Region	Target/Notes
8/25	01: 08/24/2019 22:11		Survey of Luzon	Checkout; Profile over TCCON site
8/27	02: 08/27/2019 00:05		W. of Luzon	Altocumulus layers; Warm convection; MBL transects
8/30	03: 08/29/2019 22:26		Sulu Sea	Land breeze convection east of Palawan Island
8/31	04: 08/30/2019 22:49		S. Sulu Sea	Radiation profiles; Borneo emissions before burning event
9/4	05: 09/04/2019 00:02		S. Sulu Sea	Radiation profiles; ship emissions; Borneo emissions early in burning event
9/7	06^{r}: 09/06/2019 23:56	LR1-1^{r}: 9/7/2019 0:48 LR1-2^{r}: 9/7/2019 6:29	W. of Luzon	Borneo smoke; warm convection from monsoon enhancement
9/9	07$^{r\#}$: 09/08/2019 23:59	LR2$^{r\#}$: 9/9/2019 0:52	E. of Luzon & *R/V Sally Ride*	CB outflow boundary; warm clouds; Ac sampling & profile over Sally Ride
9/10		LR3$^{r\#}$: 9/10/2019 0:41:15	*R/V Sally Ride*	Convection observed by the SeaPOL radar
9/13		LR4: 9/13/2019 5:28	*R/V Sally Ride*	Convection observed by the SeaPOL radar
9/14	08: 09/13/2019 20:42		Luzon Strait & Manila	Early morning radiation & MBL; Aeolus verification; Manila remote sensing
9/15		LR5$^{r\#}$: 9/15/2019 7:32	E. of Luzon & *R/V Sally Ride*	Convection observed by the SeaPOL radar

9/16	09: 09/15/2019 21:55		Sulu Sea	Dense Borneo smoke and warm cloud sampling from monsoon enhancement
9/17	10[r]: 09/16/2019 21:57	LR6-1[r]: 9/17/2019 0:40 LR6-2[r]: 9/17/2019 4:24	E. of Luzon	Dense Borneo smoke entering deep convection; Mt Mayon emissions
9/20	11[*]: 09/19/2019 22:47	LR7[*]: 9/20/2019 1:18	N. of Luzon	Warm convergence line induced by TY Tapah
9/21		LR8: 9/21/2019 23:45	*R/V Sally Ride*	Convection observed by the SeaPOL radar
9/22	12[#]: 09/21/2019 22:28		E. of Luzon & *R/V Sally Ride*	Fair weather clouds and warm convection
9/24	13[*#]: 09/23/2019 23:55	LR9[*#]: 9/24/2019 6:15	E. of Luzon & *R/V Sally Ride*	Fair weather cu and warm convection
9/25	14[*]: 09/25/2019 02:55	LR10[*]: 9/25/2019 4:26	E. of Luzon	Fair weather clouds and island spawned deep convection
9/28	15: 09/27/2019 20:34		N. of Luzon	Morning radiation and fair weather clouds; Aeolus verification
9/29	16[*]: 09/29/2019 02:28	LR11[*]: 9/29/2019 2:54	E. of Luzon	Convergence line induced by TY Mitag
10/2	17: 10/1/2019 21:40		E. of Luzon	Morning convection; fair weather clouds; Asian emissions
10/4	18: 10/03/2019 22:55		Manila	Metro Manila super plume
10/5	19: 10/5/2019 01:31		W. of Luzon	Fair weather convection outside of mesoscale low

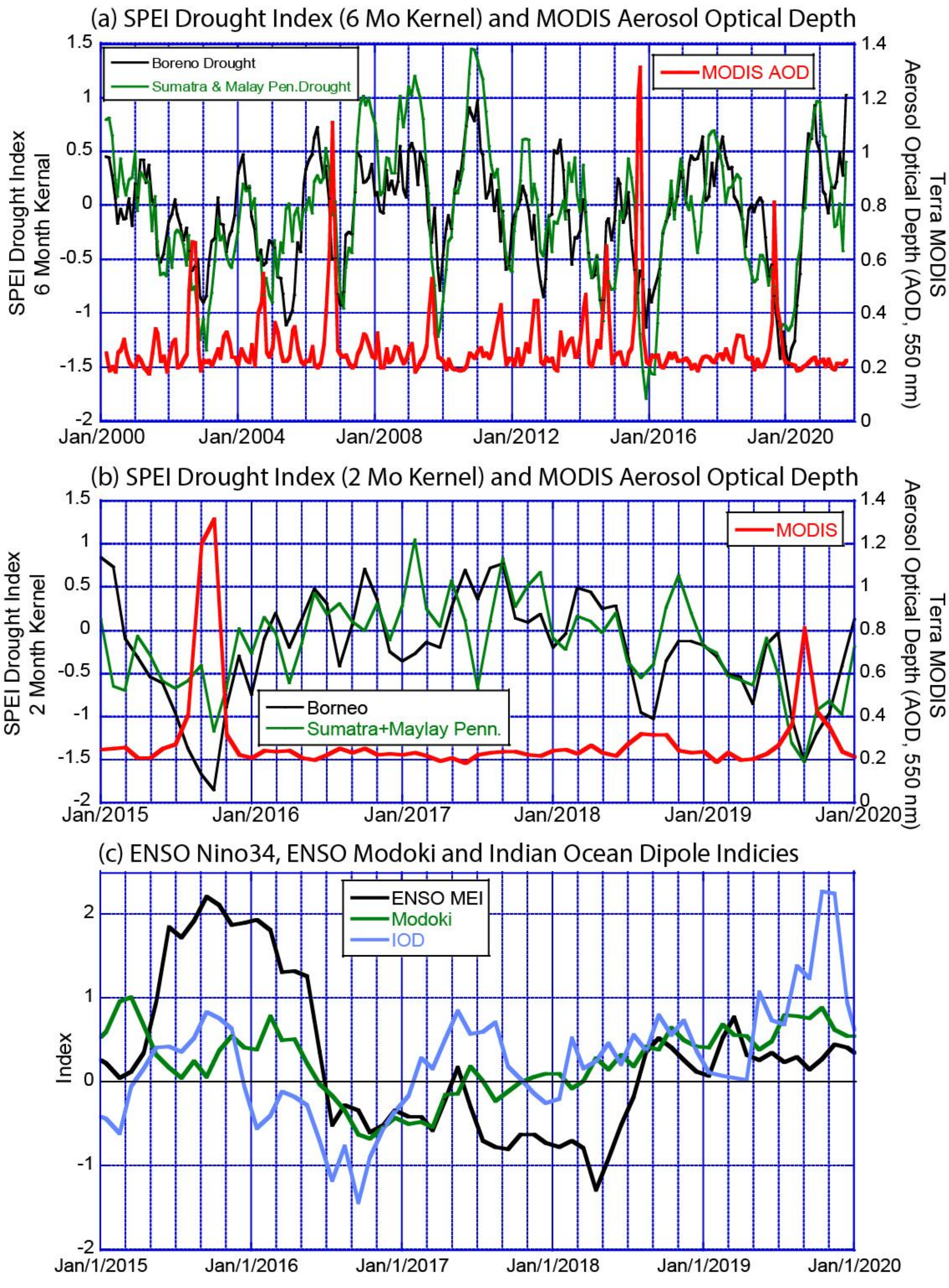

Figure S.1.1. Time series of key climate variables to help place the 2019 CAMP2Ex campaign season in context. (a) a 22 year time series of the SPEI drought index with a 6 month averaging kernel for two bounding boxes for Borneo (6 S to 8 N; 108E to 120E); and Sumatra +the Malaya Peninsula (6 S to 8 N; 95E to 108E). Also included is the average Terra MODIS monthly average Aerosol Optical Depth (550 nm) over that combined area (6 S- 8 N; 95 E-120 E). (b) Same as (a) but zoomed for 2015 through 2019 and a 2 month averaging kernel for the SPEI drought products. (c) Key tropical indices for 2015 through 2019 including the Multivariate ENSO Index Version 2 (MEIv2) for ENSO, for El Niño Modoki, and the JMA/JAXA DMI product Indian Ocean Dipole.

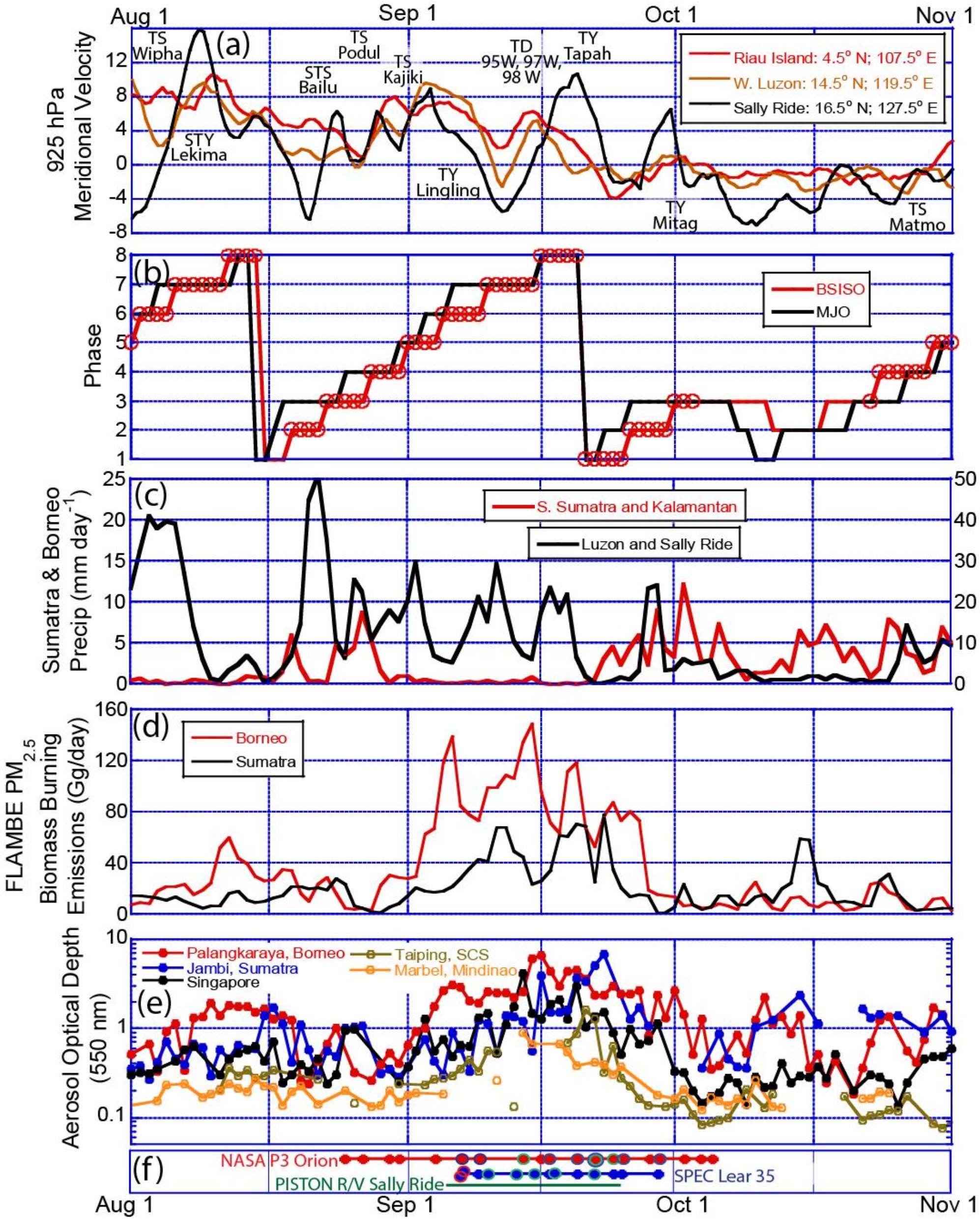

Figure S.1.2. Time series of key environmental parameters relevant to the CAMP^{2}Ex study domain from August through October 2019. Included are (a) 925 hPa ERA5 meridional velocity as an indicator of monsoonal strength for three locations, and markers for tropical disturbances that passed west of 130 E; b) MJO and BSISO phase, with additional markers for when the amplitude was >1; c) IMERG derived precipitation for boxes containing Borneo and Sumatra (6S-8N; 95-120E), and Luzon and a portion of the NWTP out to the Sally Ride operations area(10-20N; 117-130E); (d) daily FLAMBE (Reid et al., 2009; Hyer et al., 2013) estimates of biomass burning emissions for the islands of Borneo and Sumatra; (e) AERONET interpolated 550nm AOD for sites with operational data during the mission; and (f) flight days for the P-3 (Red) and Learjet 35 (Blue), and PISTON R/V Sally Ride on-station sampling period (Green), with a secondary outer circle indicating coordinated observations with the other assets.

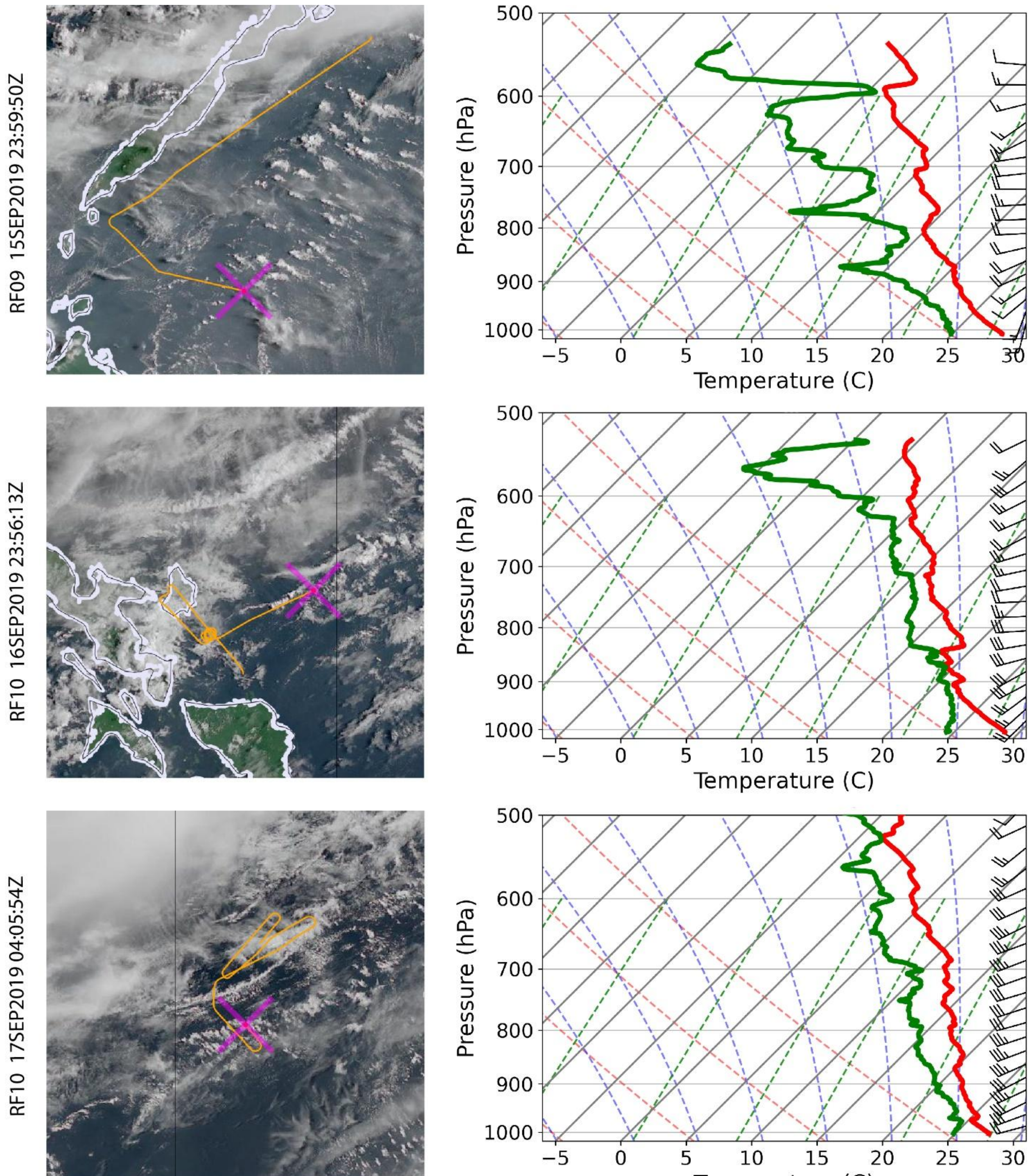

Figure S.1.3. Supplemental satellite images and soundings associated with Figure 1 (c), (d), and (e) Sept. 16-17 2019 biomass burning emissions case in the main body of this paper. Soundings, grey-temperature; red-dry adiabat; blue-wet adiabat. Satellite AHI true color image at the time of dropsonde release.

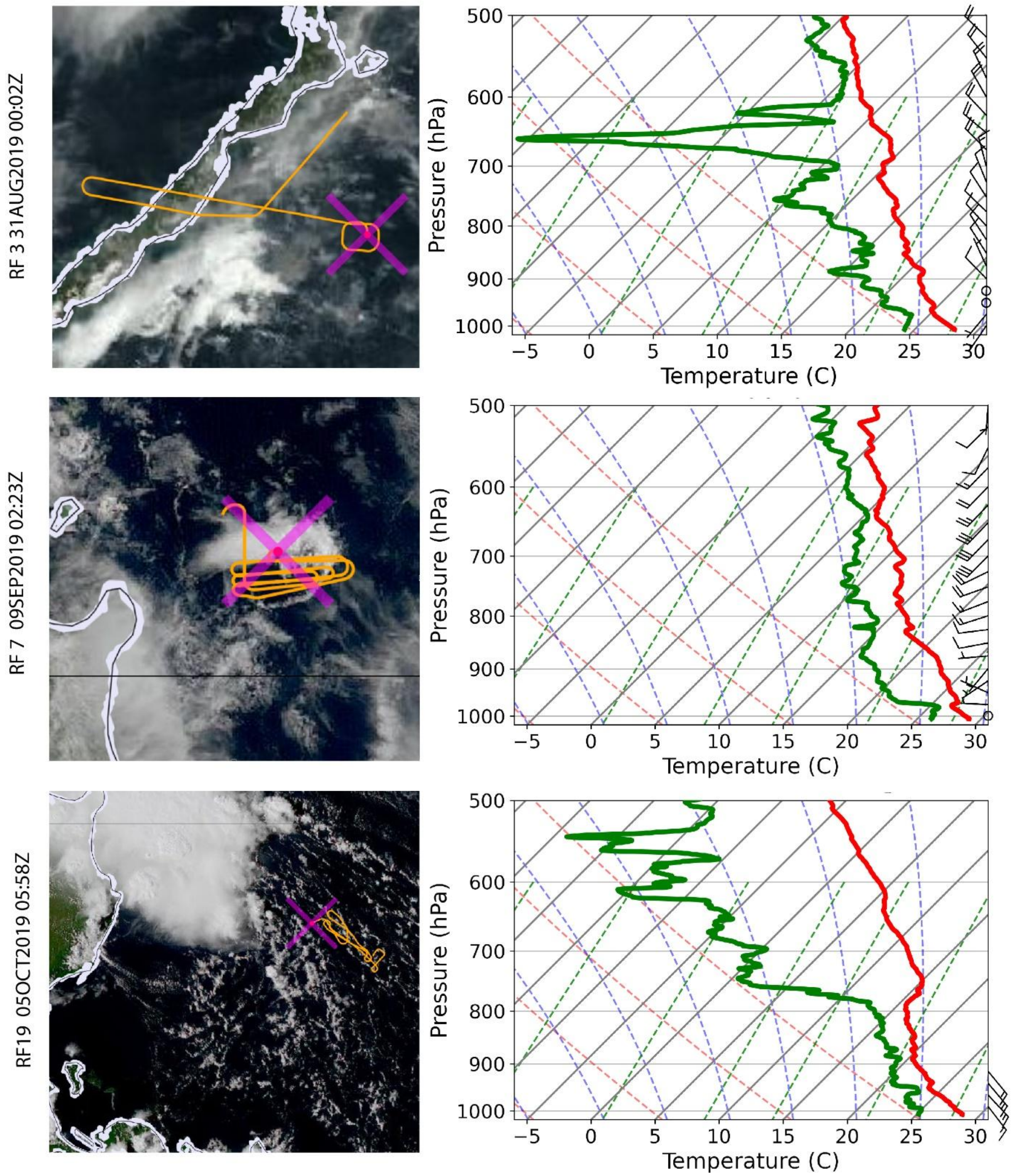

Figure S.1.4. Same as Figure S.1.3 but with supplemental satellite images and soundings associated with the Figure 1 (f), (g) and (h). These correspond to environments related to sea breeze convection from Palawan Island (Aug. 30 2019); Cold pool formation from isolated deep convection (Sept 9, 2019); and post monsoon congestus (Oct. 5, 2019), respectively.

Supplemental Section S.2: Mission instrumentation

The NASA P-3 and SPEC Learjet 35 were instrumented for atmospheric characterization specifically to help integrate aerosol lifecycle, clouds/precipitation and radiation research areas whereas the Manila Observatory was instrumented to provide a longer term record of the metro Manila environment. This supplemental section provides references to the airborne payloads and the Manila observatory supersite in a series of short descriptions and tables. As noted in the main body of the paper, data is all available at the NASA Langley airborne data archive (https://www-air.larc.nasa.gov/missions/camp2ex/index.html) with the collection associated with doi: 10.5067/Suborbital/CAMP2EX2018/DATA001

S.2.1 The NASA P-3

The CAMP^{2}Ex science goals required the NASA P3 to perform both regional characterization as well as detailed measurements of atmospheric, aerosol, cloud, precipitation and radiative states. Therefore, while the P-3 was heavily instrumented for remote sensing for use at altitude to provide large scale context of the aerosol and cloud environment, in situ instrumentation for more detailed characterization of the column and the cloud environment were carried as well. A listing of aircraft navigation, attitude and in situ state instruments are listed in Table S.2.1, instruments used for remote sensing and the dropsonde system in Table S.2.2, in situ aerosol microphysics, aerosol optics, and aerosol and gas chemistry in Table S.2.3, and cloud microphysics in Table S.2.4. While the references included in these tables provide comprehensive instrument descriptions, brief reviews are provided for the core remote sensors and aerosol instruments. Cloud and precipitation probes on the P-3 were also included on the Learjet 35 and are discussed in more detail in S.2.2

S.2.1.1 The High Spectral Resolution Lidar

The NASA Langley HSRL-2 instrument, which was deployed on the P-3 for CAMP2Ex, uses the HSRL technique to independently retrieve aerosol and tenuous cloud extinction and backscatter (Hair et al., 2008; Burton et al., 2018). This instrument uses the HSRL technique at 355 and 532 nm and the standard backscatter technique at 1064 nm to derive these parameters. Particulate depolarization is measured at all three wavelengths. Approximate horizontal and vertical resolutions are ($\Delta x \sim 1.5$ km, $\Delta z \sim 15$ m) for aerosol backscatter, depolarization, and aerosol backscatter wavelength dependence (i.e. Ångström exponent for aerosol backscatter) for two wavelength pairs (355-532 and 532-1064). The corresponding resolutions for aerosol extinction and aerosol extinction-to-backscatter ratio at 355 and 532 nm are ($\Delta x \sim 9$ km, $\Delta z \sim 150$ m). These resolutions can be varied depending on conditions and the required specific analyses. HSRL-2 derived products include estimates of Planetary Boundary Layer (PBL) heights, which are identified as sharp gradients in aerosol backscatter profiles (Scarino et al., 2014). Additionally, an aerosol type identifier (i.e., urban, maritime, polluted marine, pure dust, dusty mix, smoke, fresh smoke, and ice) is inferred at the resolution of the extinction products via an aerosol classification algorithm that uses the HSRL-2 measurements of depolarization, aerosol extinction/backscatter ratio, and aerosol backscatter wavelength dependence (Burton et al., 2012).

S.2.1.2 Airborne Third Generation Precipitation Radar (APR3)

The JPL APR-3 instrument, which was deployed on the P-3 for CAMP2Ex, is a Ku-/Ka-/W-band Doppler cloud and Doppler precipitation radar with cross-track scanning capability between ±25˚ degrees cross-track. Some elements of APR-3 can also be configured differently to meet the specific needs of a particular airborne mission within the hosting aircraft capabilities: for CAMP^{2}EX APR-3 was configured to deliver Linear Depolarization Ratio measurements at Ku-band, and high sensitivity co-polar nadir measurements at W-band. APR-3 adopts High Power Amplifiers at all bands and pulse compression at Ku and Ka band. The fundamental products of APR-3 are calibrated and geolocated radar reflectivity measurements at all bands as well as mean Doppler velocity line of sight measurements. Products are delivered at a number of resolutions depending on the specific radar modes: in general, the range resolutions span from 30 to 500 m, and the horizontal resolutions are consistent with real aperture antennas with beamwidths ranging from 1˚ (W-band high gain nadir antenna) to 4 - 6˚ (for the three bands of the scanning antenna). The radar sensitivity is also variable depending on the adopted mode and range from aircraft, and an example of sensitivity curves is shown in Dzambo et al. (2019). Geophysical variables that have been derived from these quantities span from hydrometeor classification, precipitation detection and quantification, vertical (and in specific situations horizontal) velocity, and microphysical retrievals. Examples of recent data products and science results that include detailed APR-3 analysis include Heymsfield et al., (2017); Tridon et al., 2019; Zagrodnik et al., 2019; Sy et al., 2020, and Turk et al., 2020.

S.2.1.3 Advanced Microwave Precipitation Radiometer (AMPR)

AMPR is a cross-track-scanning (-45° to +45° relative to nadir) microwave radiometer with four frequencies: 10.7, 19.35, 37.1, and 85.5 GHz, and two orthogonally polarized channels per frequency. AMPR's scene polarization varies as a function of scan angle, from pure vertical (V) polarization on the left edge of the scan (relative to aircraft direction) varying to pure horizontal (H) by the right edge for the A channel, and the opposite for the B channel (Amiot et al. 2021). Relevant to CAMP^{2}Ex, AMPR's frequencies are sensitive to clouds and precipitation, atmospheric water vapor, and ocean surface winds.

For the AMPR installation on the P-3B, a radome was required. During post-processing, the influence of the radome was removed from the observations, and the mixed-polarization observations were deconvolved to pure H and V inputs. In addition, retrievals of cloud liquid water path, total atmospheric water vapor content, and ocean surface wind speed were produced following the Amiot et al. (2021) methodology modified for the tropical atmosphere. These retrievals were validated against other CAMP^{2}Ex observations (e.g., dropsondes) and they provide reasonable error characteristics. All AMPR products are available on the CAMP^{2}Ex data archive, and imagery is available on the Jet Propulsion Laboratory (JPL) CAMP^{2}Ex portal. AMPR was down for Science Flight (SF) #1, and full-polarization retrievals are available for SF #5-19. SF #2-4 have brightness temperature observations from all four frequencies but some channels experienced partial outages, so no additional retrievals were performed for those SFs.

S.2.1.4 The Research Scanning Polarimeter (RSP)

Cloud properties are inferred from data of the Research Scanning Polarimeter (RSP, Cairns et al., 2003). The RSP observes multi-angle total and polarized reflectances in nine spectral bands centered at 410, 470, 550, 670, 865, 960, 1590, 1880, and 2260 nm. The RSP scans along the aircraft track taking samples at 0.8° viewing angle intervals, with additional calibration measurements being made at the end of each scan. RSP's field of view is about 14 mrad, leading to pixel sizes of about 10 to 50 m for typical separations between aircraft and the surface or cloud top of 1 to 4 km, respectively. Data files (level 1B) are provided containing all observations obtained per scan. In addition, data files (level 1C) are provided that contain measurements taken at different times, but collocated on a single footprint on the target (surface of cloud top).

Level 2 data files are provided containing derived cloud and aerosol products. Cloud top heights are inferred from the observed multi-angle parallax (Sinclair et al. 2015). Effective radii and variance of the drop size distribution at tops of liquid and mixed-phase clouds are retrieved using multi-angle polarimetry (Alexandrov et al. 2012a, 2012b). In addition, droplet effective radii are also retrieved, simultaneously with cloud optical thickness, using the bi-spectral approach (Nakajima and King, 1990). For non-cloudy scenes above ocean, aerosol spectral optical depth, complex refractive index, single-scattering albedo, layer height and the effective radius and variance of the aerosol size distribution for the fine- and coarse-mode aerosols are retrieved (Stamnes et al. 2018). The aerosol number concentration is inferred from the aerosol optical depth and layer height (Schlosser et al. 2022). The ocean surface roughness, which is proportional to wind speed, and the chlorophyl-a concentration are also simultaneously retrieved. For these data, observations of 21 scans are averaged, leading to temporal and spatial resolutions of about 18 seconds and 2 km, respectively. For both cloudy and clear scenes the column water vapor amount is estimated using both total and polarized reflectance observations in the 960 nm band, which is in a water vapor absorption band, and the 865 nm band (Stamnes et al. 2018). These water vapor estimates have been used as part of the estimation of droplet number concentration (Sinclair et al. 2019).

S.2.1.5 Airborne Vertical Atmospheric Profiling System (AVAPS)

The Airborne Vertical Atmospheric Profiling System (AVAPS) is a dropsonde system developed by the National Center for Atmospheric Research (NCAR). The system is comprised of three primary components: (1) a launch rack containing the computer which operates the system, telemetry hardware, and launcher operation switches; (2) the dropsondes themselves, which are deployable tubes that contain a pressure, temperature, and relative humidity (PTH) sensor, GPS hardware for vertical location and horizontal winds, and a parachute; and (3) a launch tube (usually at the rear of the aircraft in use) containing a GPS re-radiator where the dropsondes are placed immediately prior to launch. When a sonde is launched, the parachute deploys within seconds, after which the dropsonde falls to the surface at approximately 10 m/s and transmits PTH information (2 Hz) and GPS position/winds information (4 Hz) until hitting the ocean surface. Vaisala RD41 dropsondes are presently in use, which include the Vaisala RSS421 pressure, temperature, and humidity sensor module and an independent GPS receiver used to calculate winds and fall speed.

Basic operation requires first initializing a dropsonde by connecting it to the computer and subsequently purging impurities from the PTH sensor. Then, the dropsonde can be configured for use by re-connecting it to the computer via the hardware rack's umbilical cable and tuning it to a user-selected telemetry radio frequency. Once a telemetry frequency has been set, the dropsonde is placed in the tube to prepare for launch, where it obtains a GPS lock from the in-tube reradiator prior to launch. To launch the sonde, the "ARM" switch on the hardware rack must be on, and the "LAUNCH" switch is activated to open the bottom hatch of the launch tube and deploy the sonde. Pressure differentials between the cabin and outside help to force the sonde out of the launch tube, after which parachute deployment and GPS transmission should occur within seconds with ideal operation.

The P3 released 197 sondes during CAMP2Ex, ranging from 6-13 per flight. The data yield was high, with only a handful of minor QA/QC issues. The most significant issue was a late or missing lock on GPS position and winds due to a broken cable during the first half of the mission. This significantly delayed the acquisition of position and wind measurements, with a median GPS acquisition time of 32 seconds. Fifty percent % of soundings report proper GPS position and winds 500 m below flight level, with GPS availability increasing to about 80% at 2.5 km above ground level, and more than 98 % in the lowest 500 m above the surface. The second issue was a slight but consistent bias (around -1.99 hPa in R0 data) in the AVAPS pressure readings when compared to the P-3 at the same GPS altitude within an hour of launch. The pressure sensors are themselves known to have a slight negative offset of -0.56 hPa, but this was corrected in the raw data and would not explain the entirety of the observed bias. Lastly, about 4 drops of the 197 successful launches of the campaign were "fast fall" launches that had improper parachute deployment. This left over 97% of launches with proper deployment of the parachute.

S.2.1.6 Turbulent Air Motion Measurement System (TAMMS)

Fast-response and high-frequency measurements of the three-dimensional wind field, temperature, and pressure was made with the Turbulent Air Motion Measurement System (TAMMS; Barrick et al., 1996, Thornhill et al., 2003). The P-3 TAMMS configuration includes fast-response flow-angle and temperature sensors, aircraft inertial data, and a real-time data acquisition system to record the incoming signals at a rate between 100 and 200 Hz. The flow-angle system includes five, flush mounted pressure-ports installed in a cruciform pattern on the radome to provide the angles of attack (AOA) and sideslip (SSLIP). As a backup / redundancy, we also have heated Rosemount 858Y probes mounted on the side and top of the fuselage to provide an additional measurement of the angles of attack and sideslip. Corresponding fast response, high-precision pressure transducers are placed as close as possible to the pressure ports to minimize the introduction of time delays. Pitch and yaw maneuvers, speed variations and reverse headings are required periodically during deployments to verify system operation and for calibration/validation of the inputs required to compute the 3-dimensional winds utilizing the full air motion equations (Lenschow, 1986). Ambient air temperature measurements needed to determine the P-3 true air speed and for deriving heat fluxes are made with a Rosemount Model 102 non-deiced total air temperature sensor with a fast response platinum sensing element (E102E4AL). This sensor has been shown in previous field missions to provide real fluctuations at great than 5 Hz resolution. Archived data products include the 3-dimensional wind field (u, v, w, and wind speed/direction), ambient temperature, pressure and dew point, and aircraft position / attitude (latitude, longitude, altitude, pitch, roll, heading). Post-mission analysis products of momentum fluxes as well as latent and sensible heat fluxes were created to aid in boundary layer analysis efforts.

S.2.1.7 The Langley Aerosol Research Group Experiment (LARGE)

Aerosol microphysical, optical, and chemical properties were measured by a suite of commercial instrumentation extensively modified for airborne operation and tailored to CAMP2Ex science objectives (Table S.2.3). Three particle sizers were used to measure particle size distributions from 0.003 to 5 μm diameter (i.e., up to the cutpoint of the sample inlet), each with significant size overlap with the Fast Integrated Mobility Spectrometer (FIMS) to provide redundancy and additional information content from complimentary analytic techniques (e.g., mobility vs. optical or aerodynamic sizing). Total (with diameters greater than 3nm and 10nm) and non-volatile (at 350C, diameters greater than 10nm) particle concentrations are also measured to corroborate integrated particle size distributions and to quantify ultrafine particle concentrations and new particle formation. Bulk aerosol scattering and absorption coefficients were measured at three visible wavelengths and are used to calculate secondary aerosol properties such as single scattering albedo, Angstrom exponents, and scattering hygroscopicity for validation of remote-sensing observations and retrievals. Aerosol chemical composition is measured by three complimentary techniques: a Particle-into-Liquid Sampler (PILS), High-Resolution Time-of-Flight Aerosol Mass Spectrometer (HR-ToF-AMS), and Single Particle Soot Photometer (SP2). Together these observations provide a comprehensive view of both refractory (e.g., black carbon and sea-salt) and non-refractory (e.g., sulfate and organic) particle composition with a time response from several minutes (i.e., for PILS) and to 1-Hz (i.e., for HR-ToF-AMS and SP2).

With a focus on aerosol-cloud interactions, identical analytic techniques employed for PILS samples (i.e., ion chromatography and water-soluble organic carbon analysis) were also utilized for cloud water samples collected with a custom Axial Cyclone Cloud-water Collector (AC3) to explore aqueous processing and wet scavenging processes. Concentrations of cloud condensation nuclei (CCN) were also explicitly measured at relevant cloud supersaturations.

S.2.1.8 Trace Gas Measurements

A suite of trace gas instruments was deployed on NASA's P-3 to measure H_2O(v), CO, CO_2, CH_4, O_3, SO_2, NO, NO_x, and NO_y. Water vapor was measured by the NASA Langley Diode Laser Hygrometer (Diskin, et al., 2002; Podolske, et al., 2003), an open-path near-infrared absorption spectrometer configured specifically for operation on the P-3B aircraft. This instrument utilizes an external optical path between a zenith port-mounted optical transceiver and a retroreflector installed on the aircraft's vertical tail. The instrument operates on one of three isolated spectral lines of differing strengths to provide good signal to noise and precision over the wide dynamic range of water vapor present in the measurement domain. From the native ~100 Hz temporal sampling, data were averaged to 1 Hz and 20 Hz to align with other instrument measurement frequencies. Measurement accuracy and precision are 5% and 0.1% (1 sigma, 1 sec), respectively.

The carbon species were measured by a near-infrared cavity ringdown spectrometer (G2401-m, Picarro, Inc.) with a custom sampling system to improve airborne performance (DiGangi et al., 2021). Measurements were reported at 0.4 Hz, with concentrations traceable to the WMO X2014A (CO), X2007 (CO_2), and X2004A (CH_4) scales. Ozone was measured with a UV dual-beam absorption spectrometer (Model 205, 2B Technologies, Inc.) also with a custom sampling system to improve high altitude performance (Wei et al., 2021). Ozone measurements were reported at 0.5 Hz, with intermittent zeroing in flight to correct for baseline drift, and calibrated before and after the campaign using a NIST-traceable ozone calibration source (Model 306, 2B Technologies, Inc.).

The nitrogen species were measured using a modified two-channel Air Quality Design (AQD), Inc., high sensitivity NO_x instrument, using O_3 chemiluminescence (CL) to detect NO and photolysis and CL to measure NO_2 on one channel and a heated molybdenum converter installed upstream of the second channel's sample line for NO_y measurement. NO_y was continuously measured while NO and NO_x sampled serially every 30s using a single detector. The NO measurement was interpolated and subtracted from NO_x mode to correct the NO_2 fraction for photocell conversion efficiency. NO_x was then calculated by adding back NO. For continuous SO_2 measurement a pulsed fluorescence instrument was used. Both nitrogen species and SO_2 measurements were sampled from a pressure controlled inlet.

S.2.2.The SPEC Learjet 35

The SPECc Learjet 35 was equipped to characterize active convection from cloud base to top, especially for those clouds penetrating above the P-3's 8 km MSL service ceiling. The Learjet 35 was also tasked with flying beneath the P-3 to help interpret and verify the P-3's APR3 radar. Included were state, liquid/ice water, and microphysics probes to characterize cloud cores, precipitation and ice formation. These included an overlapping range of sampling sizes from aerosol CN and fine mode size to small cloud droplets to precipitation, and droplet and ice crystal imaging, with identical makes of instruments included on the P3 when possible. A listing of SPEC 35 instrumentation is provided in Table S.2.5.

S.2.3 The Manila Observatory Supersite

To provide context to the airborne mission, a 2018 through early 2020 CAMP^{2}Ex weatHer and Composition Monitoring (CHECSM) effort was initiated. A supersite was established at the Manila Observatory (MO), an urban mixed background site in Quezon City on the grounds of Ateneo de Manila University (14.64 N; 121.08 E). This site is within the Metro -Manila mega-city (also known as the National Capital Region of the Philippines), which is composed of 16 cities and 1 municipality and a total with a total population of the surrounding area of over 13.5 million (Philippine Statistics Authority, 2020). Long-term particulate pollution measurements at the Manila Observatory site showed that the National Capital Region's fine particulate matter concentration ($PM_{2.5}$) has been exceeding the annual guideline values set by the World Health Organization (Cruz et al., 2019, Simpas et al., 2014, Kim Oanh et al., 2006) with significant contribution from black carbon (Alas et al., 2017, Kecorius et al., 2017, Cruz et al., 2019, Simpas et al., 2014, Kim Oanh et al., 2006). While much of the observed pollution in Metro Manila is from local emissions with 88% contribution from the transportation sector (DENR - EMB, 2015), evidences of long-range transport of pollution aided by southwesterly flow and low precipitation were also observed through the CHECSM effort (Braun et al., 2020, Stahl et al., 2020). This context is important for CAMP^{2}Ex, as the study region is impacted not only by emissions from urban environments but also by other aerosol sources including emission from Borneo and the marine environment. The CHECSM site provided an organization structure to be a laboratory for urban air quality and weather assessment, provide a study location for local, maritime and long range transport contributions to the Manila aerosol environment. It is used to evaluate satellite and model products in a heavily urbanized environment in a Southeast Asia environment, and to serve as a laboratory for urban air quality and weather assessment. CHECSM also provided research opportunities to students, allowing for hands-on experience with world class research instrumentation.

The MO site has hosted an Aerosol Robotic Network (AERONET; Holben et al., 2018) site since 2009, although due to prevalent cirrus and had no data yields for August –Sept 22 2019 during the SWM portion of the airborne IOP. A listing of instruments deployments specifically for CHECSM is provided in Table S.2.6. Given the high cirrus prevalence in the region, for baseline aerosol monitoring as part of CHECSM, the NASA CALIOP science team supported the deployment of the University of Wisconsin High Spectral Resolution Lidar (HSRL) to monitor aerosol and cloud layers. Alongside, was surface radiation instrumentation including broadband IR and solar irradiances, and direct/diffuse solar radiation. Solar spectral radiation and direct/diffuse mid-visible radiation was also measured to retrieve column aerosol and cloud column optical thickness and thus complement HSRL. Extensive surface sampling of aerosol properties was conducted at the Manila Observatory in association with the University of Arizona and NRL as were a host of surface weather observations. Of particular interest was diurnally varying and size resolved aerosol chemistry and black carbon within the megacity.

References:

Alas, H. D., Müller, T., Birmili, W., Kecorius, S., Cambaliza, M. O., Simpas, J. B., Cayetano, M., Weinhold, K., Vallar, E.,Galvez, M. C., and Wiedensohler, A., 2017: Spatial Characterization of Black Carbon Mass Concentration in the Atmosphere of a Southeast Asian Megacity: An Air Quality Case Study for Metro Manila, Philippines, Aerosol. Air Qual. Res., 18, 2301–2317, https://doi.org/10.4209/aaqr.2017.08.0281.

Alexandrov, M. D., Cairns, B., Emde, C., Ackerman, A. S., & van Diedenhoven, B., 2012a: Accuracy assessments of cloud droplet size retrievals from polarized reflectance measurements by the research scanning polarimeter. Remote Sensing of Environment, 125, 92–111, doi:10.1016/j.rse.2012.07.012.

Alexandrov, M.D., B. Cairns, and M.I. Mishchenko, 2012b: Rainbow Fourier transform. J. Quant. Spectrosc. Radiat. Transfer, 113, 2521-2535, doi:10.1016/j.jqsrt.2012.03.025.

Alexandrov, M.D., B. Cairns, K. Sinclair, A.P. Wasilewski, L. Ziemba, E. Crosbie, R. Moore, J. Hair, A.J. Scarino, Y. Hu, S. Stamnes, M.A. Shook, and G. Chen, 2018: Retrievals of cloud droplet size from the research scanning polarimeter data: Validation using in situ measurements. Remote Sens. Environ., 210, 76-95, doi:10.1016/j.rse.2018.03.005.

Amiot, C. G., S. K. Biswas, T. J. Lang, and D. I. Duncan, 2021: Dual-polarization deconvolution and geophysical retrievals from the Advanced Microwave Precipitation Radiometer during OLYMPEX/RADEX. J. Atmos. Oceanic Technol., 38, 607 – 628, https://doi.org/10.1175/JTECH-D-19-0218.1.

Badosa, J., Wood, J., Blanc, P., Long, C. N., Vuilleumier, L., Demengel, D., and Haeffelin, M., 2014: Solar irradiances measured using SPN1 radiometers: uncertainties and clues for development, Atmos. Meas. Tech., 7, 4267–4283, https://doi.org/10.5194/amt-7-4267-2014

Barrick, J. D. W., Ritter, J. A., Watson, C. E., Wynkoop, M. W., Quinn, J. K., & Norfolk, D. R.(1996): Calibration of NASA turbulent air motion measurement system, NASA Tech. Pap. TP-310, NASA, Washington, D. C..

Baumgardner, D. and A. Rodi, 1989: Laboratory and Wind Tunnel Evaluations of the Rosemount Icing Detector. *J. Tech.*, 970-979, doi.org/10.1175/1520-0426(1989)006<0971:LAWTEO>2.0.CO;2

Beswick, K. M., M. W. Gallagher, A. R. Webb, E. G. Norton, and F. Perry, 2008: Application of the Aventech AIMMS20AQ airborne probe for turbulence measurements during the Convective Storm Initiation Project. *Atmos. Chem. Phys*., 8, 5449–5463, doi:10.5194/acp-8-5449-2008.

Beyersdorf, A., L. Ziemba, G. Chen, C. Corr, J. Crawford, G. Diskin, R. Moore, K. L. Thornhill, E. Winstead, and B. Anderson, 2016: The impacts of aerosol loading, composition, and water uptake on aerosol extinction variability in the Baltimore–Washington, D.C. region. *Atmos. Chem. Phys.*, **16**, 1003-1015, doi:10.5194/acp-16-1003-2016.

Braun, R. A., Aghdam, M. A., Bañaga, P. A., Betito, G., Cambaliza, M. O., Cruz, M. T., Lorenzo, G. R., MacDonald, A. B., Simpas, J. B., Stahl, C., and Sorooshian, A., 2020: Long-range aerosol transport and impacts on size-resolved aerosol composition in Metro Manila, Philippines, Atmos. Chem. Phys., 20, 2387–2405, https://doi.org/10.5194/acp-20-2387-2020.

Brenguier, J.-L., T. Bourrianne, A. de Araujo Coelho, J. Isbert, R. Peytavi, D. Trevarin, and P. Wechsler, 1998: Improvements of droplet size distribution measurements with the Fast-FSSP. *J. Atmos. Oceanic Technol.*, 15, 1077–1090, doi:10.1175/1520-0426(1998)015,1077:IODSDM.2.0.CO;2

Brooks, I. M., 2003: Finding boundary layer top: Application of a wavelet covariance transform to lidar backscatter profiles, *J Atmos Ocean Tech*, *20*(8), 1092-1105.

Bucholtz, A., D. L. Hlavka, M. J. McGill, K. S. Schmidt, P. Pilewskie, S. M. Davis, E. A. Reid, and A. L. Walker, 2010: Directly Measured Heating Rates of a Tropical Subvisible Cirrus Cloud, *J. Geophys. Res*., 115, D00J09, doi:10.1029/2009JD013128.

Burton, S. P., Ferrare, R. A., Hostetler, C. A., Hair, J. W., Rogers, R. R., Obland, M. D., Butler, C. F., Cook, A. L., Harper, D. B., and Froyd, K. D., 2012: Aerosol classification using airborne High Spectral Resolution Lidar measurements - methodology and examples, *Atmospheric Measurement Techniques*, *5*(1), 73-98.

Burton, S. P., C. A. Hostetler, A. L. Cook, J. W. Hair, S. T. Seaman, S. Scola, D. B. Harper, J. A. Smith, M. A. Fenn, R. A. Ferrare, P. E. Saide, E. V. Chemyakin, and D. Müller, 2018: Calibration of a high spectral resolution lidar using a Michelson interferometer, with data examples from ORACLES, Appl Optics, 57, 6061-6075, https://doi.org/10.1364/AO.57.006061, 2018

Cai, Y., J. R. Snider, and P. Wechsler, 2013: Calibration of the passive cavity aerosol spectrometer probe for airborne determination of the size distribution. *Atmos. Meas. Tech*., **6**, 2349–2358, doi:10.5194/amt-6-2349-2013.

Cairns, B., Russell, E. E., LaVeigne, J., & Tennant, P., 2003: Research scanning polarimeter and airborne usage for remote sensing of aerosols. In J. A. Shaw, & J. S. Tyo (Eds.), Polarization science and remote sensing, Proc. SPIE. Volume 5158, Polarization Science and Remote Sensing, https://doi.org/10.1117/12.518320

Chase, R. J., J. A. Finlon, P. Borque, G. M. McFarquhar, S. W. Nesbitt, S. Tanelli, O. O. Sy, S. L. Durden, M. R. Poellot, 2018: Evaluation of triple-frequency radar retrieval of snowfall properties using coincident airborne in situ observations during OLYMPEX. Geophysical Research Letters, 45, 5752–5760. https://doi.org/10.1029/2018GL077997

Cober, S. G., G. A. Isaac, A. V. Korolev, and J. W. Strapp, 2001: Assessing Cloud-Phase Conditions. *J. Appl. Meteor.,* 40, 967-1983, doi.org/10.1175/1520-0450(2001)040<1967:ACPC>2.0.CO;2

Crosbie, E., M. Brown, M. Shook, L. Ziemba, R. Moore, T. Shingler, E. Winstead, K. L. Thornhill, C. Robinson, A. MacDonald, H. Dadashazar, A. Sorooshian, A. Beyersdorf, A. Eugene, J. Collett Jr., D. Straub, and B. Anderson, 2018: Development and characterization of a high-efficiency, aircraft-based axial cyclone cloud water collector. *Atmos. Meas. Tech.*, **11**, 5025-5048, https://doi.org/10.5194/amt-11-5025-2018.

Cruz, M. T., Bañaga, P. A., Betito, G., Braun, R. A., Stahl, C., Aghdam, M. A., Cambaliza, M. O., Dadashazar, H., Hilario, M. R., Lorenzo, G. R., Ma, L., MacDonald, A. B., Pabroa, P. C., Yee, J. R., Simpas, J. B., and Sorooshian, A., 2019: Size-resolved composition and morphology of particulate matter during the southwest monsoon in Metro Manila, Philippines, Atmos. Chem. Phys., 19, 10675–10696, https://doi.org/10.5194/acp-19-10675-2019.

Dzambo AM, L'Ecuyer T, Sy OO, Tanelli S. The observed structure and precipitation characteristics of southeast Atlantic stratocumulus from airborne radar during ORACLES 2016–17. Journal of Applied Meteorology and Climatology. 2019 Oct;58(10):2197-215.

DeCarlo, P., E. Dunlea, J. Kimmel, A. Aiken, D. Sueper, J. Crounse, P. Wennberg, L. Emmons, Y. Shinozuka, A. Clarke, J. Zhou, J. Tomlinson, D. Collins, D. Knapp, A. Weinheimer, D. Montzka, T. Campos, and J. Jimenez, 2008: Fast airborne aerosol size and chemistry measurements above Mexico City and Central Mexico during the MILAGRO campaign. *Atmos. Chem. Phys.*, **8**, 4027-4048, https://doi.org/10.5194/acp-8-4027-2008.

DeMott, P., T. Hill, M. Petters, A. Bertram, Y. Tobo, R. Mason, K. Suski, C. McCluskey, E. Levin, G. Schill, Y. Boose, A. Rauker, A. Miller, J. Zaragoza, K. Rocci, N. Rothfus, H. Taylor, J. Hader, C. Chou, J. Huffman, U. Poschl, A. Prenni, and S. Kreidenweis, 2017: Comparative measurements of ambient atmospheric concentrations of ice nucleating particles using multiple immersion freezing methods and a continuous flow diffusion chamber. *Atmos. Chem. Phys*., **17**, 11227–11245, https://doi.org/10.5194/acp-17-11227-2017.

Department of Environment and Natural Resources Environmental Management Bureau (DENR – EMB, Philippine). 2015. National air quality status report 2008 – 2015, Available online: https://emb.gov.ph/national-air-quality-status-report/

DiGangi, J.P., Choi, Y., Nowak, J.B., Halliday, H.S., Diskin, G.S., Feng, S., Barkley, Z.R., Lauvaux, T., Pal, S., Davis, K.J., Baier, B.C., Sweeney, C., 2021: Seasonal Variability in Local Carbon Dioxide Biomass Burning Sources over the Central and Eastern US using Airborne In Situ Enhancement Ratios. *J. Geophys. Res.: Atmos.*, **in press**, e2020JD034525. https://doi.org/10.1029/2020JD034525

Diskin, G. S., J. R. Podolske, G. W. Sachse, and T. A. Slate, 2002: Open-Path Airborne Tunable Diode Laser Hygrometer, SPIE Proceedings Volume 4817, Diode Lasers and Applications in Atmospheric Sensing, https://doi.org/10.1117/12.453736

DMT PCASP Manual, DOC-0228, Rev C. http://www.dropletmeasurement.com/resources/manuals-guides.

Dzambo, A.M., T. L'Ecuyer, O.O. Sy, and S. Tanelli, 2019: The Observed Structure and Precipitation Characteristics of Southeast Atlantic Stratocumulus from Airborne Radar during ORACLES 2016–17. *J. Appl. Meteor. Climatol.,* **58**, 2197–2215, https://doi.org/10.1175/JAMC-D-19-0032.1

Eloranta, E. W.. 2005: High spectral resolution lidar, in *Lidar: Range-Resolved Optical Remote Sensing of the Atmosphere*, edited by K. Weitkamp, Springer, New York.

Fast, J. D., et al., 2012: Transport and mixing patterns over Central California during the carbonaceous aerosol and radiative effects study (CARES), *Atmos. Chem. Phys.*, *12*(4), 1759-1783.

Froyd, K., D. Murphy, C. Brock, P. Campuzano-Jost, J. Dibb, J-L. Jimenez, A. Kupc, A. Middlebrook, G. Schill, K. L. Thornhill, C. Williamson, J. Wilson, and L. Ziemba, 2019: A new method to quantify mineral dust and other aerosol species from aircraft platforms using single-particle mass spectrometry. *Atmos. Meas. Tech*, **12**, 6209-6239, https://doi.org/10.5194/amt-12-6209-2019.

Guan, H., B. Schmid, A. Bucholtz, and R. Bergstrom, 2010: Sensitivity of shortwave radiative flux density, forcing, and heating rate to the aerosol vertical profile, J. Geophys. Res., 115, D06209.

Haggerty, J. A., J. A. Maslanik, and J. A. Curry, 2003: Heterogeneity of sea ice surface temperature at SHEBA from aircraft measurements, *J. Geophys. Res.*, 108(C10), 8052, doi:10.1029/2000JC000560.

Hair, J. W., C. A. Hostetler, A. L. Cook, D. B. Harper, R. A. Ferrare, T. L. Mack, W. Welch, L. R., Izquierdo, F. E. Hovis, 2008: Airborne High Spectral Resolution Lidar for Profiling Aerosol Optical Properties, *Applied Optics*, 47,doi: 10.1364/AO.47.006734.

Heymsfield, A., Bansemer, A., Wood, N.B., Liu, G., Tanelli, S., Sy, O.O., Poellot, M., and Liu C. (2017): Toward Improving Ice Water Content and Snow Rate Retrievals from Radars Part II: Results From Three Wavelength Radar /Collocated In Situ Measurements and CloudSat/GPM/TRMM Radar Data. *J. Appl. Meteor. Climatol., early online release,* https://doi.org/10.1175/JAMC-D-17-0164.

Hock, T. F., Franklin, J. L. 1999: The NCAR GPS Dropwindsonde. Bull. Amer. Meteor. Soc., 80, 407-420.

Kecorius, S., Madueno, L., Vallar, E., Alas, H., Betito, G., Birmili, W., Cambaliza, M. O., Catipay, G., Gonzaga-Cayetano, M., Galvez, M. C., Lorenzo, G., Muller, T., Simpas, J. B., Tamayo, E. G., and Wiedensohler, A., 2017: Aerosol particle mixing state, refractory particle number size distributions and emission factors in a polluted urban environment: Case study of Metro Manila, Philippines, Atmos. Environ., 170, 169–183, https://doi.org/10.1016/j.atmosenv.2017.09.037.

Kim Oanh, N. T., Upadhyay, N., Zhuang, Y. H., Hao, Z. P., Murthy, D. V. S., Lestari, P., Villarin, J. T., Chengchua, K., Co, H. X., Dung, N. T., and Lindgren, E. S., 2016: Particulate air pollution in six Asian cities: Spatial and temporal distributions, and associated sources, Atmos. Environ.,40, 3367–3380, https://doi.org/10.1016/j.atmosenv.2006.01.050.

Kley, D., and M. McFarland, 1980: Chemiluminescence detector for NO and NO2. *Atmos. Technol.*, **12**, 63-69.

Korolev, A. V., Strapp, J. W., Isaac, G. A., & Nevzorov, A. N., 1998: The Nevzorov Airborne Hot-wire LWC-TWC Probe: Principle of operation and performance characteristics. *Journal of Atmospheric and Oceanic Technology*, *15*(6), 1495–1510. https://doi.org/10.1175/1520-0426(1998)015<1495:TNAHWL>2.0.CO;2

Knollenberg, R. G., 1981: Techniques for probing cloud microstructure. Clouds: Their Formation, Optical Properties, and Effects. P.V. Hobbs and A. Deepak, Eds., *Academic Press*, 15–91, doi:10.1016/B978-0-12-350720-4.50007-7.

Kulkarni, P., and J. Wang, 2006: New fast integrated mobility spectrometer for real-time measurement of aerosol size distribution - I: Concept and theory. *J. Aerosol Sci.*, **37,** 1303-1325.

Lawson, R. P. and W. A. Cooper, 1990: Performance of some airborne thermometers in clouds. *J. Atmos. Oceanic Technol.*, 7, 480–494, doi:10.1175/1520-0426(1990)007,0480:POSATI.2.0.CO;2.

Lawson, R. P., R. E. Stewart, J. W. Strapp, G. A. Isaac, 1993: Aircraft observations of the origin and growth of very large snowflakes. *Geophys. Res. Lett.*, 20(1), doi.org/10.1029/92GL02917.

Lawson, R. P., R. E. Stewart, and L. J. Angus, 1998: Observations and numerical simulations of the origin and development of very large snowflakes. *J. Atmos. Sci*., 55, 3209–3229.

Lawson, R. P., B. A. Baker, C. G. Schmitt, and T.L. Jensen, 2001: An overview of microphysical properties of Arctic stratus clouds observed during FIRE.ACE. *J. Geophys. Res.*, **106(D14)**, 14989-15014.

Lawson, R. P., D. O'Connor, P. Zmarzly, K. Weaver, B. A. Baker, Q. Mo, and H. Jonsson, 2006: The 2D-S (stereo) probe: Design and preliminary tests of a new airborne, high speed, highresolution particle imaging probe. *J. Atmos. Oceanic Technol*., 23, 1462–1477, doi:10.1175/JTECH1927.1.

Lawson, R. P., C. Gurganus, S. Woods, and R. Bruintjes, 2017: Aircraft Observations of Cumulus Microphysics Ranging from the Tropics to Midlatitudes: Implications for "New" Secondary Ice Process. *J. Atmos. Sci***., 74,** 2899-2920.

LeBlanc, S. E., Pilewskie, P., Schmidt, K. S., and Coddington, O.(2015): A spectral method for discriminating thermodynamic phase and retrieving cloud optical thickness and effective radius using transmitted solar radiance spectra, Atmos. Meas. Tech., 8, 1361–1383, https://doi.org/10.5194/amt-8-1361-2015.

Lenschow, D. H. (1986): Probing the Atmospheric Boundary Layer, Am. Meteorol. Soc., Boston, Mass.

Liu, W., S. L. Kaufman, B. L. Osmondson, G. J. Sem, F. R. Quant, D. R. Oberreit, 2006: Water-based Condensation Particle Counters for Environmental Monitoring of Ultrafine Particles, *Journal of Air and Waste Management Association*, 56(4):444-455.

Long, C. N., A. Bucholtz, H. Jonsson, B. Schmid, A. Vogelmann, and J. Wood, 2010: A Method of Correcting for Tilt from Horizontal in Downwelling Shortwave Irradiance Measurements on Moving Platforms, *The Open Atmospheric Science Journal*, 4, 78, DOI: 10.2174/1874282301004010078

Luke, W. T., 1997: Evaluation of a commercial pulsed fluorescence detector for the measurement of low-level SO2 concentrations during the Gas-Phase Sulfur Intercomparison Experiment. *J. Geophys. Res: Atmos.*, **102**, D13. 16255-16265, https://doi.org/10.1029/96JD03347

Marmorino, G. O., G.B. Smith, R. P. North, B. Baschek 2018: Application of Airborne Infrared Remote Sensing to the Study of Ocean Submesoscale Eddies , *Front. Mech. Eng.*, *https://doi.org/10.3389/fmech.2018.00010*

Mason, B., N. Wagner, G. Adler, E. Andrews, C. Brock, T. Gordon, D. Lack, A. Perring, M. Richardson, J. Schwarz, M. Shook, K. L. Thornhill, L. Ziemba, and D. Murphy, 2018: An intercomparison of aerosol absorption measurements conducted during the SEAC4RS campaign. *Aerosol Sci. Tech.*, **9**, 1012-1027, https://doi.org/10.1080/02786826.2018.1500012.

Masuda, R.; Iwabuchi, H.; Schmidt, K.S.; Damiani, A.; Kudo, R., 2019: Retrieval of Cloud Optical Thickness from Sky-View Camera Images using a Deep Convolutional Neural Network based on Three-Dimensional Radiative Transfer. Remote Sens. 11, 1962.

McNaughton, C. A. Clarke, S. Howell, M. Pinkerton, B. Anderson, K. L. Thornhill, C. Hudgins, E. Winstead, J. Dibb, E. Scheuer, and H. Maring, 2007: Results from the DC-8 Inlet Characterization Experiment (DICE): Airborne Versus Surface Sampling of Mineral Dust and Sea Salt Aerosols. *Aerosol Sci. Tech.*, **41**, 136-159, https://doi.org/10.1080/02786820601118406.

Moore, R., K. L. Thornhill, B. Weinzierl, D. Sauer, E. D'Ascoli, J. Kim, M. Lichtenstern, M. Scheibe, B. Beaton, A. Beyersdorf, J. Barrick, D. Bulzan, C. Corr, E. Crosbie, T. Jurkat, R. Martin, D. Riddick, M. Shook, G. Slover, C. Voigt, R. White, E. Winstead, R. Yasky, L. Ziemba, A. Brown, H. Schlager, and B. Anderson, 2017: Biofuel blending reduces particle emissions from aircraft engines at cruise conditions. *Nature*, **543**, 411-415, https://doi.org/10.1038/nature21420.

Moore, R. and A. Nenes, 2009: Scanning flow CCN analysis – A method for fast measurements of CCN spectra. *Aerosol Sci. Tech.*, **43**, 1192-1207, https://doi.org/10.1080/02786820903289780.

Müller, D., C. A., Hostetler, R. A., Ferrare, S. P., Burton, E. Chemyakin, A. Kolgotin, J. W. Hair, A. L. Cook, D. B. Harper, R. R. Rogers, R. W. Hare, C. S. Cleckner, M. D. Obland, J. Tomlinson, L. K. Berg, and B. Schmid, 2014: Airborne multiwavelength High Spectral Resolution Lidar (HSRL-2) observations during TCAP 2012: vertical profiles of optical and microphysical properties of a smoke/urban haze plume over the northeastern coast of the US, Atmos. Meas. Tech. 7, 3487-3496, doi:10.5194/amt-7-3487-2014.

Nakajima, T., & King, M. D., 1990: Determination of the optical thickness and effective particle radius of clouds from reflected solar radiation measurements. Part I: Theory. Journal of the Atmospheric Sciences, 47, 1878–1893

Norgren, M. S., J. Wood, K. S. Schmidt, B. van Diedenhoven, S. A. Stamnes, L. D. Ziemba, E. C. Crosbie, M. A. Shook, A. S. Kittelman, S. E. LeBlanc, S. Broccardo, S. Freitag, and J. S. Reid, 2022: Above-aircraft cirrus cloud and aerosol optical depth from hyperspectral irradiances measured by a total-diffuse radiometer, Atmos. Meas. Tech., 15, 1373–1394, https://doi.org/10.5194/amt-15-1373-2022, 2022.

O'Connor, D., B. Baker, and R. P. Lawson, 2008: Upgrades to the FSSP-100 Electronics. 15th. Int. Conf. on Clouds and Precipitation. Cancun, Mexico, Universidad Nacional Autónoma deMéxico, P13.6. [Available online at http://cabernet.atmosfcu.unam.mx/ICCP-2008/abstracts/Program_on_line/Poster_13/OConnor_extended_final.pdf.]

Peltier, R., R. Weber, and A. Sullivan, 2008: Investigating a liquid-based method for online organic carbon detection in atmospheric Schmidt, K. S., and P. Pilewskie, 2011: Airborne Measurements of Spectral Shortwave Radiation in Cloud and Aerosol Remote Sensing and Energy Budget Studies, in Light Scattering Reviews, 6, A. Kokhanovsky (ed.), Springer.particles. *Aerosol Sci. Tech.*, **41**, 1117-1127, https://doi.org/10.1080/02786820701777465.

Philippine Statistics Authority, 2020a:. Highlights of the National Capital region (NCR) Population 2020 Census of Population and Housing (2020 CPH). https://psa.gov.ph/content/highlights-national-capital-region-ncr-population-2020-census-population-and-housing-2020#:~:text=The%20population%20of%20the%20National,the%20Philippine%20population%20in%202020.

Podolske, J. R., G. W. Sachse, and G. S. Diskin, 2003, Calibration and data retrieval algorithms for the NASA Langley/Ames Diode Laser Hygrometer for the NASA Transport and Chemical Evolution Over the Pacific (TRACE-P) mission, *J. Geophys. Res.*, 108, 8792, doi:10.1029/2002JD003156, D20.

Rutledge, S. A., Chandrasekar, V., Fuchs, B., George, J., Junyent, F., Dolan, B., Kennedy, P. C., & Drushka, K. (2019). SEA-POL Goes to Sea, Bulletin of the American Meteorological Society, 100, 2285-2301, https://journals.ametsoc.org/view/journals/bams/100/11/bams-d-18-0233.1.xml.

Scarino, A.J., Obland, M. D., Fast, J. D., Burton S. P., Ferrare, R.A., Hostetler C. A., Berg, K., Lefer, B., Haman, C., Hair, J. W., Rogers, R. R., Butler, C., Cook, A. L., Harper, D. B., 2014: Comparison of mixed layer heights from Airborne High Spectral Resolution Lidar, Ground-based Measurements, and the WRF-Chem Model during CalNex and CARES, Atmos. Chem and Phys., 14, 5547-5560.6.

Schlosser, J.S., S. Stamnes, S.P. Burton, B. Cairns, E. Crosbie, B. Van Diedenhoven, G. Diskin, S. Dmitrovic, R. Ferrare, J.W. Hair, C.A. Hostetler, Y. Hu, X. Liu, R.H. Moore, T. Shingler, M.A. Shook, K.L. Thornhill, E. Winstead, L. Ziemba, and A. Sorooshian, 2022: Polarimeter + lidar-derived aerosol particle number concentration. Front. Remote Sens., 3, 885332, doi:10.3389/frsen.2022.885332.

Schmidt K.S., Wendisch M., Kindel B. (2021) Airborne Solar Radiation Sensors. In: Foken T. (eds) Springer Handbook of Atmospheric Measurements. Springer Handbooks. Springer, Cham. https://doi.org/10.1007/978-3-030-52171-4_40

Simpas, J., Lorenzo, G., and Cruz, M. T., 2014: Monitoring Particulate Matter Levels and Composition for Source Apportionment Study in Metro Manila, Philippines, in: Improving Air Quality in Asian Developing Countries: Compilation of Research Findings, edited by: Kim Oanh, N. T., NARENCA, Vietnam Publishing House of Natural Resources, Environment and Cartography, Vietnam, 239–261.

Sinclair, K., B. van Diedenhoven, B. Cairns, J. Yorks, A. Wasilewski, and M. McGill, 2017: Remote sensing of multiple cloud layer heights using multi-angular measurements. Atmos. Meas. Tech., 10, 2361-2375, doi:10.5194/amt-10-2361-2017.

Sinclair, K., B. van Diedenhoven, B. Cairns, M. Alexandrov, R. Moore, E. Crosbie, and L. Ziemba, 2019: Polarimetric retrievals of cloud droplet number concentrations. Remote Sens. Environ., 228, 227-240, doi:10.1016/j.rse.2019.04.008.

Sorooshian, A., F. Brechtel, Y. Ma, R. Weber, A. Corless, R. Flagan, and J. Seinfeld, 2006: Modeling and Characterization of a Particle-into-Liquid Sampler (PILS). *Aerosol Sci. Tech.*, **6**, 396-409, https://doi.org/10.1080/02786820600632282.

Stahl, C., Crosbie, E., Bañaga, P. A., Betito, G., Braun, R. A., Cainglet, Z. M., Cambaliza, M. O., Cruz, M. T., Dado, J. M., Hilario, M. R. A., Leung, G. F., MacDonald, A. B., Magnaye, A. M., Reid, J., Robinson, C., Shook, M. A., Simpas, J. B., Visaga, S. M., Winstead, E., Ziemba, L., and Sorooshian, A., 2021: Total organic carbon and the contribution from speciated organics in cloud water: airborne data analysis from the CAMP^{2}Ex field campaign, Atmos. Chem. Phys., 21, 14109–14129, https://doi.org/10.5194/acp-21-14109-2021.

Stahl, C., Cruz, M.T., Bañaga, P.A. *et al.* , 2020: An annual time series of weekly size-resolved aerosol properties in the megacity of Metro Manila, Philippines. *Sci Data,* **7,** :128, https://doi.org/10.1038/s41597-020-0466-y

Stamnes, S., C. Hostetler, R. Ferrare, S. Burton, X. Liu, J. Hair, Y. Hu, A. Wasilewski, W. Martin, B. van Diedenhoven, J. Chowdhary, I. Cetinic, L. Berg, K. Stamnes, and B. Cairns, 2018: Simultaneous polarimeter retrievals of microphysical aerosol and ocean color parameters from the "MAPP" algorithm with comparison to high spectral resolution lidar aerosol and ocean products. Appl. Opt., 57, no. 10, 2394-2413, doi:10.1364/AO.57.002394.

Thornhill, K. L., B. E. Anderson, J. D. W. Barrick, D. R. Bagwell, R. Friesen, and D. H. Lenschow, 2003: Air motion intercomparison flights during Transport and Chemical Evolution in the Pacific (TRACE-P)/ACE-ASIA, J. Geophys. Res., 108(D20), 9001,doi:10.1029/2002JD003108

Sy, O. O., Tanelli, S., Durden S. L., Heymsfield, A., Bansemer, A., Kuo K.S, Niamsuwan, N., Beauchamp, R.M., Chandrasekar, V., Vega, M., Johnson M.P. Impact of mass–size parameterizations of frozen hydrometeors on microphysical retrievals: Evaluation by matching radar to in situ observations from GCPEx and OLYMPEx. Journal of Atmospheric and Oceanic Technology. 2020 May 28;37(6):993-1012.

Tridon F., Battaglia, A., Chase, R. J., Turk F.J., Leinonen, J., Kneifel, S., Mroz, K., Finlon, J., Bansemer, A., Tanelli S., Heymsfield A. J. The microphysics of stratiform precipitation during OLYMPEX: Compatibility between triple-frequency radar and airborne in situ observations. Journal of Geophysical Research: Atmospheres. 2019 Aug 16;124(15):8764-92.

Turk F.J., Hristova-Veleva S., Durden, S. L., Tanelli, S., Sy, O., Emmitt, G. D., Greco, S., Zhang, S. Q. (2020) Joint analysis of convective structure from the APR-2 precipitation radar and the DAWN Doppler wind lidar during the 2017 Convective Processes Experiment (CPEX). Atmospheric Measurement Techniques. 2020 Aug 21;13(8):4521-37.

Wang, Z., A. Sorooshian, G. Prabhakar, M. Coggon, and H. Jonsson, 2014: Impact of emissions from shipping, land, and the ocean on stratocumulus cloud water elemental composition during the 2011E-PEACE field campaign. Atmos. Environ., **89**, 570-580, https://doi.org/10.1016/j.atmosenv.2014.01.020.

Wei, Y., Shrestha, R., Pal, S., Gerken, T., Feng, S., McNelis, J., Singh, D., Thornton, M.M., Boyer, A.G., Shook, M.A., Chen, G., Baier, B.C., Barkley, Z.R., Barrick, J.D., Bennett, J.R., Browell, E.V., Campbell, J.F., Campbell, L.J., Choi, Y., Collins, J., Dobler, J., Eckl, M., Fiehn, A., Fried, A., Digangi, J.P., Barton-Grimley, R., Halliday, H., Klausner, T., Kooi, S., Kostinek, J., Lauvaux, T., Lin, B., McGill, M.J., Meadows, B., Miles, N.L., Nehrir, A.R., Nowak, J.B., Obland, M., O'Dell, C., Fao, R.M.P., Richardson, S.J., Richter, D., Roiger, A., Sweeney, C., Walega, J., Weibring, P., Williams, C.A., Yang, M.M., Zhou, Y., Davis, K.J., 2021: Atmospheric Carbon and Transport – America (ACT-America) Data Sets: Description, Management, and Delivery. *Earth Space Sci.*, **8**, e2020EA001634. https://doi.org/10.1029/2020EA001634

Wu, L., O. Hasekamp, B. van Diedenhoven, B. Cairns, J. E. Yorks, and J. Chowdhary (2016), Passive remote sensing of aerosol layer height using near-UV multiangle polarization measurements, Geophys. Res. Lett., 43, 8783–8790, doi:10.1002/2016GL069848.

Pollack, I.B., B.M. Lerner, and T.B. Ryerson, 2010: Evaluation of ultraviolet light-emitting diodes for detection of atmospheric NO2 by photolysis-chemiluminescence. *J. Atmos. Chem.,* **65**, 111-125, https://doi.org/10.1007/s10874-011-9184-3.

Wang, J., M. Pikridas, S. R. Spielman, and T. Pinterich, 2017: A fast integrated mobility spectrometer for rapid measurement of sub-micrometer aerosol size distribution, Part I: Design and model evaluation. *J. Aerosol Sci.*, **108,** 44-55.

Wang, Y., T. Pinterich, and J. Wang, 2018: Rapid measurement of sub-micrometer aerosol size distribution using a fast integrated mobility spectrometer. *J. Aerosol Sci.*, **121,** 12-20.

Williams, E. J., K. Baumann, J.M. Roberts, S.B. Bertman, R.B. Norton, F.C. Fehsenfeld, S.R. Springston, L.J. Nunnermacker, L. Newman, K. Olszyna, J. Meagher, B. Hartsell, E. Edgerton, J.R. Pearson, and M.O. Rodgers, 1998: Intercomparison of ground-based NOy measurement techniques. *J. Geophys. Res.*, **103**, 22261-22280, https://doi.org/10.1029/JD092iD12p14710.

Woods, S., P. Lawson, E. Jensen, T. Thornberry, A. Rollins, P. Bui, L. Pfister, M. Avery, 2018: Microphysical Properties of Tropical Tropopause Layer Cirrus. *J. Geophys. Res. Atmos.*, doi: 10.1029/2017JD028068.

Yoneyama, K., and Zhang, C., 2020: Years of the Maritime Continent. *Geophysical Research Letters*, 47, e2020GL087182. https://doi.org/10.1029/2020GL087182

Zagrodnik, J. P., McMurdie L. A., Houze Jr, R. A., Tanelli S. Vertical structure and microphysical characteristics of frontal systems passing over a three-dimensional coastal mountain range. Journal of the Atmospheric Sciences. 2019 Jun;76(6):1521-46.

Ziemba, L., K. L. Thornhill, R. Ferrare, J. Barrick, A. Beyersdorf, G. Chen, S. Crumeyrolle, J. Hair, C. Hostetler, C. Hudgins, M. Obland, R. Rogers, J. J. Scarino, E. Winstead, and B. Anderson, 2013: Airborne observations of aerosol extinction by in situ and remote-sensing techniques: Evaluation of particle hygroscopicity. *Geophys. Res. Lett.*, **40**, 417– 422, doi:10.1029/2012GL055.

Table S2.1 Navigation, state and radiation instrumentation data carried onboard the NASA P-3; NSRC: NASA's National Suborbital Research Center; TAMMS: turbulent air motion measurement system. Uncertainties are estimates, as they have complex proportion depending on the environment.

Parameter	**Instrument**	**Uncertainty**	**PI**	**Reference**
Position & Attitude	Northrop Grumman Litton 251 EGI	~5 m SEP; 0.01 deg.	NSRC	N/A
Radar Altitude	APN 232	100 ft.	Facility	N/A
Temperature	Rosemount 102E4AL type non-deiced	0.5 deg C	NSRC	N/A
Dew Point	Edgetech Vigilant 3-Stage hygrometer	0.2 deg C	NSRC	N/A
Wind Speed/Direction	Litton 251 EGI & Avionics	1 ms^{-1}; 0.5 deg	NSRC	N/A
Water Vapor Mixing Ratio	Diode Laser Hygrometer (DLH)	5%	Diskin (LaRC)	Diskin (2002), Podolske (2003)
Derived Relative Humidity	Diode Laser Hygrometer (DLH), TAMMS	15%	Diskin (LaRC), Thornhill (SSAI/LaRC)	Diskin (2002), Podolske (2003), Thornhill et al., 2003.
P, T, 3-D Winds (u, v, w, WSPD, WDIR), fluxes	TAMMS		Thornhill (SSAI/LaRC)	Thornhill et al., 2003.
Broadband solar irradiance: downwelling and upwelling	Modified Kipp & Zonen CM22 pyranometers	4%	Bucholtz (NPS)	Bucholtz et al., 2010
Broadband IR irradiance: downwelling and upwelling	Modified Kipp&Zonen CG4 pyrgeometers	5%	Bucholtz(NPS)	Bucholtz et al., 2010
Diffuse and global broadband shortwave irradiance: downwelling	Sunshine Pyranometer (SPN-1; Broadband)	10%	Bucholtz (NPS)	Badosa et al. (2014)
Diffuse and global spectral shortwave irradiance: downwelling	Sunshine Pyranometer (SPN-S; Spectral)	7%	Schmidt (CU)	Norgren et al. (2022)
Above-aircraft optical thickness (500 and 670 nm)	Sunshine Pyranometer (SPN-S; Spectral)	10-20%	Schmidt (CU)	Norgren et al. (2022)
Spectral Solar irradiance: downwelling and upwelling	Solar Spectral Flux Radiometer (SSFR)	5%	Schmidt (CU)	Schmidt and Pilewskie (2011)
SST, cloud top temperatures	Heitronics KT-19.85 pyrometer	2ºC	NSRC	Haggerty et al., 2003

Table S.2.2 Remote sensing and dropsonde instruments carried onboard the P-3 used primarily when the P3 was flying at high (>5 km) altitude to characterize the regional environment. Uncertainties are estimates, as they have complex proportion depending on the environment.

Parameter	**Instrument**	**Uncertainty**	**PI**	**Reference**
Imagery				
Forward & Nadir Video	HD Full frame cameras	N/A	NSRC	
Hemispheric all-sky Images	All-sky camera (zenith-viewing)	N/A	Bucholtz (NPS)	
Hemispheric geolocated & calibrated radiance (red, green, blue)	All-sky camera (nadir-viewing)	10%	Schmidt (CU)	Masuda et al. (2019)
Brightness Temperature 3-5 µm band	FLIR SC6000 MWIR imager	20 mK	Smith (NRL)	Marmorino et al., 2018
Brightness Temperature 8-14 µm band	Sofradir ATOM1024 LWIR imager	50 mK	Smith (NRL)	Marmorino et al., 2018
Radiance 900-2500 nm, 139 bands HSI	Headwall XEVA-2.5-320	50 mK	Smith (NRL)	Marmorino et al., 2018
Lidar, Radar & Microwave				
Aerosol profiles: Extinction, Backscatter, Depolarization, Type, Effective Radius, Concentration. Column: AOD, Above-Cloud AOD, AOD apportioned by aerosol type. Mixed Layer Height (where possible from aerosol gradients).	HSRL-2 (High Spectral Resolution Lidar – Generation 2)	Extinction: 10 Mm^{-1} Backscatter: 0.2 $(Mm\text{-}sr)^{-1}$ Depolarization: 2% AOD: 0.02 Mixed Layer Height: 100 m Effective Radius: 30% Number, Surface, Volume Concentrations: 100, 30, 50%	Ferrare/Hostetler (LaRC)	Burton et al., 2018; Hair et al., , 2008 Scarino et al., 2014 Müller et al., 2014
Ka, Ku, and W band Radar Reflectivity Factor, Mean Doppler Velocity	Airborne Precipitation Radar, Third Generation (APR3)		Mace(UT)/Tanelli(JPL)	Chase et al., 2018 Dzambo et al., 2019
Microwave Brightness Temperature at 10, 19, 37, 85 GHz	Advanced Microwave Precipitation Radiometer (AMPR)	Noise equivalent delta temperature: 0.5 K Wind speed: 2 m s^{-1} Water vapor: 10% Liquid water path: 0.1 kg m^{-2}	Timothy Lang (MSFC)	Amiot et al., (2021)
Polarimetry				
Multi-angle total reflectances and degree of polarization at 410, 469, 555, 670, 864, 1594, 2264 nm	Research Scanning Polarimeter (RSP)	Reflectance: 3%; Degree of polarization: 0.2%	van Diedenhoven/Cairns (NASA GISS)	Cairns et al. 2003
Cloud top height, Cloud optical thickness, cloud top droplet effective radius, cloud top droplet effective variance	Research Scanning Polarimeter (RSP)	Eff. radius: ~1 µm; Eff. variance: ~0.02; Top height: 500m; Optical thickness: ~10% for COT<30	van Diedenhoven/Cairns (NASA GISS)	Alexandrov et al. 2012 Sinclair et al 2015 Alexandrov et al. 2018 Platnick et al. 2018
Aerosol optical depth, effective radius, effective variance, complex refractive index, single scattering albedo, number concentration, layer height	Research Scanning Polarimeter (RSP)	AOD: 0.04; Radius: 0.02 µm; Variance: 0.04; Number: ~100%; Layer height: 1km; Refr: 0.02, 0.004i; SSA: 0.03	van Diedenhoven/Cairns (NASA GISS)	Stamnes et al. 2018 Schlosser et al. 2022 Wu et al. 2016 Knobelspiesse et al. 2012

Dropsondes				
Pressure	Airborne Vertical Atmospheric Profiling System (AVAPS / Dropsondes)	±0.5 hPa	van den Heever (CSU)	Hock and Franklin 1999; UCAR/NCAR Earth Observing Laboratory 1993.
Temperature	Airborne Vertical Atmospheric Profiling System (AVAPS / Dropsondes)	±0.2 °C	van den Heever (CSU)	Hock and Franklin 1999; UCAR/NCAR Earth Observing Laboratory 1993.
Relative Humidity	Airborne Vertical Atmospheric Profiling System (AVAPS / Dropsondes)	±3%	van den Heever (CSU)	Hock and Franklin 1999; UCAR/NCAR Earth Observing Laboratory 1993.
Horizontal Wind	Airborne Vertical Atmospheric Profiling System (AVAPS / Dropsondes)	±0.5 m s^{-1}	van den Heever (CSU)	Hock and Franklin 1999; UCAR/NCAR Earth Observing Laboratory 1993.

Table S.2.3 Aerosol and gas microphysics, chemistry, and optics carried onboard the P-3. Uncertainties are estimates, as they have complex proportion depending on the environment.

Parameter	**Instrument**	**Uncertainty**	**PI**	**Reference**
Aerosol Chemistry				
Submicron non-refractory aerosol mass concentration. Cl, Organic, NH_4, NO_3, SO_4	Aerodyne High-Resolution Time-of-Flight Aerosol Mass Spectrometer	50%	Ziemba (LaRC)	DeCarlo et al. (2008)
Water-soluble mass concentration	Particle-Into-Liquid-Sampler (PILS)	30%	Crosbie (LaRC)	Sorooshian et al (2006)
Submicron refractory black carbon mass concentration	Single Particle Soot Photometer (DMT SP2)	10%	Ziemba (LaRC)	Schwarz et al (2006)
Aerosol Microphysics				
0.010 – 0.5 µm diameter mobility size	Fast integrated mobility spectrometer (FIMS)	Concentration: 15%; Size 3%	Wang (Washington U)	Kulkarni and Wang, 2006; Wang et al., 2017; 2018
0.1 – 5.0 µm diameter optical size	TSI Laser Aerosol Spectrometer	20%	Ziemba (LaRC)	Froyd et al. (2019)
0.1 - 3 µm diameter optical size	DMT Passive Cavity Aerosol Spectrometer (PCASP)	Concentration ~30%; size 25%	Lawson (SPEC)	DMT PCASP Manual, DOC-0228, Rev C. http://www.dropletmeasurement.com/resources/manuals-guides.
0.003 – 0.1µm diameter mobility size	Scanning Mobility Particle Sizer (SMPS)	20%	Ziemba (LaRC)	Moore et al. (2017)
0.7 – 5.0 µm diameter aerodynamic size	TSI Aerodynamic Particle Sizer	20%	Ziemba (LaRC)	McNaughton et al. (2007)
Total (>0.003µm) and non-volatile (350°C) particle number concentrations	TSI Condensation Particle	10%	Ziemba (LaRC)	Moore et al. (2017)
CCN number concentration and spectra	DMT Cloud Condensation Nuclei Spectrometer	5-20%	Nenes (GTech) & Weber(Cal Tech)	Moore et al. (2009)
Aerosol Optics				
Dry (RH<40%) & humidified (RH = 80%) 3 λ (450, 550, 700 nm) light scattering coefficient	Parallel humidified TSI Nephelometers	30%	Ziemba (LaRC)	Ziemba et al. (2013)
Dry 3λ (450, 550, 700 nm) light absorption coefficient	Particle Soot Absorption Photometer (PSAP)	15%	Ziemba (LaRC)	Mason et al. (2018)
Gas Chemistry				
CO_2, CO, CH_4	Picarro model G2401-m	0.1 ppm, 5 ppb, 1 ppb	Diskin (LaRC)	DiGangi, et al. (2021)
O_3	2B Technologies model 205	6 ppbv	Diskin (LaRC)	Wei, et al. (2021)

SO_2	Thermo 43i-TLE	low alt (<2.5km)=12%; high alt (2.5 to 5km) = 16%	Flynn (UH)	Luke, 1997
NO_x	Air Quality Designs, Inc. using chemiluminescence	NO=12%; NOx=14%	Flynn (UH)	Kley, andMcFarland, 1980: Pollacket al., 2010
NO_y	Air Quality Designs, Inc. using molybdenum converter	12%	Flynn (UH)	Williams, et al., 1998

S.2.4. Cloud microphysics and water chemistry carried by the NASA P-3

Parameter	Instrument	Uncertainty	PI	Reference
Cloud droplets (2-50µm)	SPEC Fast Cloud Droplet Probe (FCDP)	50%	Lawson (SPEC)	Knollenberg 1981, O'Connor et al. 2008, Lawson et al. 2017
Cloud particles (10µm–3mm)	SPEC 2D-S (Stereo) Optical Array Spectrometer	20%	Lawson (SPEC)	Lawson et al. 2006a
Cloud particles (2-50 µm)	SPEC Hawkeye-FCDP	50%	Lawson (SPEC)	Knollenberg 1981, Lawson et al. 2017; Woods et al. 2018
Cloud particles (10µm–3mm)	SPEC Hawkeye-2DS	20%	Lawson (SPEC)	Lawson et al. 2006a, Woods et al. 2018
Cloud particle habit, high res imagery	SPEC Hawkeye-CPI	10%	Lawson (SPEC)	Lawson et al. 2001, 2006b Woods et al. 2018
Precipitation (150µm – 2cm)	SPEC High Volume Precipitation Spectrometer (HVPS-3)	15%	Lawson (SPEC)	Lawson et al. 1993, 1998
Ice-Nucleating Particle Concentrations and temperature dependence	CSU Ice Spectrometer	30%	Crosbie (LaRC)/DeMott (CSU)	DeMott et al. (2017)
Water-soluble mass concentrations of common ions and organic carbon, bulk solution pH	Axial Cyclone Cloud-water Collector (AC3) Ion chromatography Sievers TOC ph electrode	30%	Crosbie (LaRC)/ Sorooshian (UA)	Crosbie et al. (2018); Stahl et al., (2021)

Table S2.5 Parameters measured on the Stratton Park Engineering Company (SPEC) Learjet 35. PI for all measurements is Paul Lawson, SPEC. Uncertainties are estimates, as they have complex proportion depending on the environment.

Parameter	Instrument	Uncertainty	Reference
State			
Temperature	Rosemount Model 102 & 510BH	0.3 C	Lawson and Cooper (1990)
Altitude	Royal Air FAA RVSM Certification	20 m	
Airspeed	Royal Air FAA RVSM Certification	1 m s^{-1}	
Dew Point Temperature	EdgeTech Chilled Mirror C-137	2 C	
Liquid Water/Total Water	Sky Tech Nevzorov LWC/TWC	0.1 g m^{-3}	Korolev et al. (1999)
Icing Rate	Rosemount Icing Rod 871LM5	N/A	Baumgardner and Rodi (1989); Cober et al. 2001
Aircraft Position	Aventech AIMMS-20 Dual GPS	10 m	Beswick et al. 2008
Aircraft Heading	Learjet Sperry Directional Gyro	1°	
Horizontal & Vertical Winds	Aventech AIMMS - 20	5°, 5 m s^{-1} 1 m s^{-1}	Beswick et al. 2008
Microphysics: Concentration, Area, Mass, Size, phase etc			
Cloud droplets (2-50 µm)	SPEC Fast Forward Scattering Spectrometer Probe (FFSSP)	50%	Knollenberg 1981, Brenguier et al. 1998, Lawson et al. 2017
Cloud droplets (2-50 µm)	SPEC Fast Cloud Droplet Probe (FCDP)	50%	Knollenberg 1981, O'Connor et al. 2008, Lawson et al. 2017
Cloud particles (10 µm – 3 mm)	SPEC 2D-S (Stereo) Optical Array Spectrometer	20%	Lawson et al. (2006a)
Cloud particles (2-50 µm)	SPEC Hawkeye-FCDP	50%	Knollenberg (1981), Lawson et al. (2017); Woods et al. (2018)
Cloud particles (10 µm – 3 mm)	SPEC Hawkeye-2DS	20%	Lawson et al. (2006a), Woods et al. (2018)
Cloud particle habit, high res imagery	SPEC Hawkeye-CPI	10%	Lawson et al. (2001, 2006b); Woods et al. (2018)
Precipitation (150 µm – 2 cm)	SPEC High Volume Precipitation Spectrometer (HVPS-3)	15%	Lawson et al. (1993, 1998)
Condensation nuclei >0.01 µm	TSI Water-based Condensation Particle Counter (CPC)	30%	Liu et al. (2006), additional references, see bibliography at: https://www.tsi.com/discontinued-products/water-based-condensation-particle-counter-3782/
Aerosol Size, 0.1 - 3 µm	DMT Passive Cavity Aerosol Spectrometer (PCASP)	30%	DMT PCASP Manual, DOC-0228, Rev C. (Cai et al., 2013) http://www.dropletmeasurement.com/resources/manuals-guides.

Table S2.6 Parameters measured at the Manila Observatory Super Site.

Parameter	Instrument	Uncertainty	PI	Reference
Aerosol profiles: Extinction, Backscatter, Depolarization, AOD, Below -Cloud AOD, AOD apportioned by aerosol type. Mixed Layer Height	High Spectral Resolution Lidar – Generation 2	Aerosol Backscatter ~10% Extinction & AOD ~ 30%	Holz (SSEC/U of Wisc)	Eloranta (2005)
Broadband Downward Solar Irradiance	Kipp&Zonen CM22 Pyranometer	4%	Bucholtz (NPS)	Bucholtz et al., 2010
Broadband Downward IR Irradiance	Kipp&Zonen CG4 pyrgeometers	5%	Bucholtz(NPS)	Bucholtz et al., 2010
Diffuse and global broadband shortwave irradiance: downwelling	Sunshine Pyranometer (SPN-1; Broadband)	10%	Bucholtz (NPS)	Badosa et al. (2014)
Diffuse and global downward shortwave irradiance (532 nm)	Sunshine Pyranometer (mid-visible; SPN-532)	10%	Schmidt (CU)	Badosa et al. (2014)
Spectral Downward Solar Irradiance (350-2150 nm) and Zenith Radiance (350-1650 nm)	Solar Spectral Flux Radiometer (SSFR) with zenith irradiance and radiance light collectors	5%	Schmidt (CU)	LeBlanc et al., 2015 Schmidt et al., 2021
Diffuse and global downward shortwave irradiance (532 nm)	Sunshine Pyranometer (SPN-532;mid-visible)	7%	Schmidt (CU)	Badosa et al. (2014) Norgren et al. (2022)
Size-resolved aerosol composition (water-soluble ions and elements) and mass	Micro-Orifice Uniform Deposit Impactor (MOUDI)	<20%, species dependent	Sorooshian (U. Arizona)	Stahl et al. (2020)

Supplemental S.3 Remote Sensing and Modeling Components

All atmospheric science campaigns rely to some extent on remote sensing and modeling systems, at the very least for daily forecasting and contextual analysis. CAMP^{2}Ex however had technology development as a core mission objective and hence significant effort was placed on integrating field observations into larger remote sensing and modeling constructs. The datasets and efforts are briefly outlined here.

S.3.1 Satellite Remote Sensing

NASA is the United States' space agency, and the CAMP^{2}Ex mission was as equally about the development of remote sensing technology and techniques for data integration as it was about the fundamental science objectives. Dozens of international satellite sensors monitor the MC's aerosol, cloud, and meteorological environments every day, and to maximize environmental characterization, CAMP^{2}Ex considered overpass schedules during flight planning. A list of satellite remote sensing products considered significant to the mission is included in Table S.3.1. Also noteworthy is the development of a satellite colocation database for the NASA P-3, SPEC Learjet 35, and the PISTON R/V Sally Ride data that is now available at the NASA Langley Airborne Archive, located on the main page (https://www-air.larc.nasa.gov/missions/camp2ex/index.html). CAMP^{2}Ex had special reliance on three classes of satellite sensors: 1) next generation Advanced Himawari Imager; 2) high resolution imagery over the maritime domain; and 3) the constellation of meteorological and climate satellites sensors. Satellite data collections from CAMP^{2}Ex that include both aircraft and ground assets are listed at the LaRC airborne data repository at (https://www-air.larc.nasa.gov/missions/camp2ex/docs/Camp2Ex_Satellite_Coordinations_for_P3_Learjet_SR_MO_by_Organization_V02.xlsx).

JMA's Advanced Himawari Imager on the Himawari-8 spacecraft (Da et al., 2015) was crucial to both the execution and the ongoing analysis phases of CAMP^{2}Ex. With many of the same channels as MODIS, AHI provides much of MODIS' retrieval capability, giving 10-minute hemispheric data, with spatial resolution like MODIS in the visible channels (0.5 km for the 0.65 um and 1 km for the rest of the visible channels). The SWIR and IR have a nominal 2 km resolution. JMA provided a dedicated AHI L1b access for the mission facilitating low latency (less than 25 minute) true color imagery, cloud, and NASA Dark Target aerosol retrievals for flight support. JMA also tasked AHI for 2.5 min rapid scan data over a northern Philippines domain for much of the mission- an important resource for object-oriented analysis and machine learning development. The NOAA Enterprise cloud retrievals based on the CLAVR-x (Heidinger et al. 2013) algorithms were processed in near-real time for mission flight planning and post mission science. The CAMP^{2}Ex AHI data record is being used for NASA aerosol and cloud geo-stationary algorithm development using the ground and aircraft measurements for validation.

Given how rapidly convection evolved in the field campaign domain, CAMP^{2}Ex aircraft needed real-time direction to appropriate targets. As commonly available imagery through standard feeds lacked the resolution, timeliness, or derived products needed, and due to concern over internet speed in the field, the CAMP2Ex remote sensing team had to develop a data flow architecture that would ensure the mission's base of operations could monitor the environment and advise the P-3 flight scientist on target opportunities, as well as ensure the safety of the aircraft. The process began at JMA, where CAMP^{2}Ex would collect AHI data through two parallel data streams: (1) the AHI data was staged at a local ftp site in Japan provided by JMA. The data was ingested into an Amazon Web Service (AWS) instance in Japan with the L1 imagery and L2 products processed using AWS with the imagery saved in the NASA Worldview format. These files where then downloaded to a server located in the aircraft hangar at Clark running a local version of NASA worldview customized to support the high temporal resolution AHI data (10 min resolution) developed by the NASA worldview software developers for the experiment; and (2) a back-up stream was processed at the Space Sciences and Engineering Center (SSEC) of University of Wisconsin-Madison using the centers near real time data archive and processing resources. A host of imagery products were generated within 10-20 minutes, and a suite of level 2 cloud and aerosol products within 30 minutes, including products utilizing recent ports of the MODIS algorithms to AHI. As discussed in Section 3 and 6, these data were and can still be viewed on the University of Wisconsin Space Science and Engineering Centers CAMP^{2}Ex specific Worldview instance (https://geoworldview.ssec.wisc.edu) as presented in Figure S.3.1. There, imagery and products would be overlaid with real time aircraft and R/V Sally Ride position and data, as well as other meteorological information, such as large-scale meteorology. To ensure data availability (as a backup stream), CAMP^{2}Ex could reach the website, but also hosted a separate instance locally in the operations center.

CAMP^{2}Ex also pushed the boundaries of spatial resolution, specially ordering satellite data collection designed for terrestrial monitoring over the maritime domain. When orbit and viewing conditions permitted, the P-3 was routed for inclusion in high resolution scenes. Cloud products operationally generated by meteorological imagers were modified for high resolution applications (e.g., Werner et al. 2016). NASA performed special data collection of the NASA/JAXA ASTER imager on the Terra spacecraft and the NASA/USGS LANDSAT-8 to cover the South China Sea through ~500 km west of the Philippines into the Northern Tropical Western Pacific. These two sensors include visible, near infrared and thermal infrared channels at resolutions better than 90 m that allow for all manner of traditional cloud retrievals including mask, height/temperature, effective radius, and liquid water path. ESA granted Sentinel 2A&B MSI collections over a similar domain. With visible and near infrared channels, Sentinel 2 can generate cloud masks, effective radius and liquid water path. The P-3 was most successful with achieving Sentinel 2 under flights, with four tight coordinations, and an additional 3 coordinations when the P-3 was in the vicinity. Finally, NGA ordered several Digital Globe/Worldview imagery with pan chromatic views at 40 cm, and single wavelengths in the visible to near infrared at 1.2, and 3.7 m shortwave IR, providing hyper resolution cloud masks. Two instances of multi-look stereographic worldview images were collected with the P-3 in the vicinity (RF 12: Sept 21, 2019 2:22; RF 17: Sept.2, 2019 2:54). Data for all of these collections can be acquired through the operational repositories from each agency.

While CAMP^{2}Ex relied on AHI for airborne operations, and specifically targeted high-resolution collections, as a matter of course the mission was supported by, and supported the development of, a host of meteorological and climate sensors. Instruments of particular importance are included in Table S.3.1, with overpasses on assets available within the aforementioned satellite coordination spreadsheet. As discussed in more detail in Section S.3.3, weather related products, particularly from microwave, radar and scatterometry as well as model data, can be viewed and downloaded on the CAMP^{2}Ex data portal (https://camp2ex.jpl.nasa.gov), with additional imagery, cloud, and aerosol products from AHI, MODIS, and VIIRS on the on the CAMP^{2}Ex geostationary site (https://geoworldview.ssec.wisc.edu). Given their wide coverage, the P-3 underflew at least one, and typically three or four imagers on each flight (e.g., MODIS on Terra and/or Aqua and SNPP and/or NOAA-20 VIIRS). For narrower swath instruments, two P-3 flights underflew ESA's Aeolus wind lidar mission (RF 8: Sept. 13, 2019 21:51 UTC and RF 15: Sept. 27, 2019 21:51 UTC respectively), one underflew GPM's precipitation radars during active convection (RF:6-Sept 7, 2019 7:01), and one under-flew the CALIPSO lidar (RF-4: Aug 31, 2019 5:36).

S.3.2 Forecasting and Modeling

As with remote sensing, CAMP^{2}Ex modeling efforts spanned operational support to detailed research focused physics studies. While there are numerous efforts underway, here we provide a short summary of datasets and efforts that are producing publically available data and/or whose publication is imminent.

Daily CAMP^{2}Ex forecasting was performed by a Manila Observatory student cohort under the supervision of Edward Fukada, retired from 30 years at the Joint Typhoon Warning Center. For operational flight planning, forecasters took a consensus approach utilizing models from numerous centers. Particularly useful for tropical forecasting were products provided by the UK Met Office Unified Model (UKMO-UM), European Center for Medium range Weather Forecasting Integrated Forecast System (ECMWF IFS) and the US Navy Global Environmental Model (NAVGEM). Corresponding charts from the UM are archived within the LaRC Airborne data repository (https://www-air.larc.nasa.gov/missions/camp2ex/index.html) as are daily charts provided by the Japan Meteorological Agency (JMA). For IFS and NAVGEM, interested investigators are directed to the ECMWF Reanalysis Version 5 (ERA5, C3S, 2017; Hersbach et al., 2020) available at Copernicus data store (https://cds.climate.copernicus.eu/#!/search?text=ERA5&type=dataset), and the Navy Archives as the US Global Oceans Data Assimilation Experiment site (US GODAE; https://usgodae.org). Tropical cyclone forecasting was central to operations and was supported by consensus products of the Automated Tropical Cyclone Forecast system (Sampson and Schrader, 2000). For mesoscale modeling, CAMP^{2}Ex made use of parallel PISTON forecasting efforts posted at https://onrpiston.colostate.edu/forecasting.html that included basin simulations from the Coupled Ocean Atmosphere Mesoscale Prediction System (Chen et al., 2010; Golaz et al., 2010). For aerosol forecasting, guidance was granted by US Navy Aerosol Analysis and Precision System (NAAPS; Lynch et al., 2016), the NASA Goddard Earth Observing System (GEOS; https://gmao.gsfc.nasa.gov/GMAO_products/NRT_products.php), and ICAP Multi Model Ensemble consensus (ICAP-MME; Session et al., 2015; Xian et al., 2019). NAAPS and ICAP-MME products are archived at the aforementioned US GODAE site.

To aid in the CAMP^{2}Ex analysis, following the intensive operations period, a retrospective global scale "mini-reanalysis" was generated for the entirety of the campaign using NASA GEOS. There are two primary benefits of this mini-reanalysis relative to the model output that was produced in NRT and used for flight planning purposes. A retrospective run allows for the use of observational data that was previously not available such as sea surface temperature and biomass burning aerosol emissions. Additionally, upgrades were implemented with respect to model physics and the Goddard Chemistry Aerosol Radiation and Transport (GOCART) aerosol module. To improve performance in tropical environments, a relaxed Arakawa Schubert convection parameterization was replaced by the scale-aware Grell-Freitas parameterization for deep convection and the University of Washington shallow convection scheme (Arnold et al., 2022). This change resulted in an improvement in the relative humidity within the lower free troposphere over the CAMP^{2}Ex domain, however a positive bias in boundary layer humidity remains (Collow et al, 2022). With respect to aerosol chemistry, the most notable update is the introduction of brown carbon and secondary organic aerosol as described in Das et al. (2021). A final version of the mini-reanalysis will include the assimilation of AOD from Himawari which is expected to improve the temporal variability of aerosols within GEOS. These updates have been implemented incrementally within GEOS. Model data has been sampled along the flight trajectories for all CAMP^{2}Ex flights (Collow et al., 2020) and is available for download at https://portal.nccs.nasa.gov/datashare/iesa/campaigns/CAMP2EX/sampled/P3B/ under GEOS-FP, in addition to flight trajectory sampled data from the Modern Era Retrospective analysis for Research and Applications, version 2 (MERRA-2).

To improve our understanding of mesoscale to microscale processes, a suite of Regional Atmospheric Modeling System (RAMS; Cotton et al., 2003; Saleeby and van den Heever 2013) simulations were performed for the team by Colorado State University at scales ranging from basin-wide to large eddy simulations (LES) (Figure S.3.2). All of the simulations described below are readily available for further use and analysis by request from the authors at Colorado State University. The long duration (~40 days) basin-scale simulations were run at high resolution (Δx ~ 1km, Δz ~ 100-300m, 5-minute output) over a large domain (1950 x 1800 x 25 km; ~5-25°N, 110-135°E) coincident with the CAMP^{2}Ex and 2019 PISTON operational areas, thereby enabling detailed analysis of convective properties over a range of thermodynamic environments (Figure S.3.2 (a)). This suite of basin-scale consists of three simulations with varying aerosol loadings as well as two additional simulations in which aerosol-radiation interactions were varied, thereby facilitating analysis of aerosol impacts at a scene-level, as well as attribution of those impacts to direct versus indirect effects (Freeman et al. 2022). Nineteen additional large-scale "forecast-like" simulations were run with a similar high resolution ($\Delta x \sim 1$km, $\Delta z \sim 100$-300m, 15-minute output) and large domain (1950 x 1800 x 25 km) to specifically examine individual P-3 flights (Figure S.3.2 (b)). These forecast-like simulations are set-up in a case-study mode initialized and nudged at the boundaries by ERA-5 reanalysis. Quick looks for these simulations are available at: https://vandenheever.atmos.colostate.edu/vdhpage/camp2ex_share/forecast-like_quicklooks/forecast-like_quicklooks.php. At the highest resolution, several suites of Large Eddy Simulations (LESs; $\Delta x \sim 100$m, $\Delta z \sim 50$-300m, 5-minute output) were run covering a mesoscale domain (150 x 150 x 17.6 km, 48 hours). These simulations were initialized using profiles derived from the aforementioned basin-scale simulations, and are thus representative of conditions in the CAMP^{2}Ex domain. The suite of high-resolution simulations included nine runs exploring the individual and combined effects of aerosol loading and static stability on trimodal convection (Sokolowsky et al., 2022). Finally, a second suite of LES ($\Delta x \sim 100$m, $\Delta z \sim 50$-200m, 5-minute output) was run over a smaller domain (100 x 100 x 15km, 48 hours), but with full representation and tracking of aerosol processes such as nucleation scavenging, evaporative regeneration, and wet deposition (Saleeby and van den Heever 2013) (Figure S.3.2 (c)). These simulations were targeted at studying the shallow cumulus and congestus modes (Leung and van den Heever, 2022), and were initialized with a combination of CAMP^{2}Ex dropsondes and ERA-5 reanalysis data. Simulations were run in which the aerosol concentration and type were varied (e.g. sulfate, absorbing carbon), and included RAMS aerosol budget capabilities, thereby facilitating analysis of aerosol impacts on convective transport and midlevel detrainment.

S.3.3 Visualization and Informatics

CAMP^{2}Ex is a highly interdisciplinary mission that must integrate and utilize the host of aforementioned satellite and model products with airborne observations. The strategy required: 1) extensive utilization of AHI geostationary datasets to direct and interpret research flights; 2) integration of satellite and model data into a visualization framework to allow for contextual analysis of the CAMP^{2}Ex analysis; and 3) development of an object oriented framework to allow for temporal consistency in data analyses.

S.3.3.1 Geoworldview

As discussed in the main body of the article and Section S.3.1, the rapid processing of AHI data was critical to CAMP^{2}Ex's ability to provide guidance to the aircraft within the study domains' rapidly evolving environment. At the same time, CAMP^{2}Ex was a pathfinder mission for the development of next generation of geostationary aerosol and cloud products. As analysis and evaluation of these products is difficult, developers needed a way to perform rapid evaluation of the environment and differences between products in a consistent manner. To meet these challenges, as part of a joint SSEC NASA Goddard Space Flight Center effort, the NASA Worldview site (https://worldview.earthdata.nasa.gov/) was modified and ported to SSEC (https://geoworldview.ssec.wisc.edu/). This site not only hosts specific CAMP^{2}Ex products, but can also tap into the primary image server that supports the primary Worldview page.

Geoworldview has the same look and feel as the primary Worldview site. Notable developments include: 1) on both Geoworldview and Worldview, the timeline supports 10 minute and custom time increments when geostationary products are activated; 2) on Geoworldview, additional layers can be displayed during the CAMP^{2}Ex mission period, including model and next generation satellite products, model layers; and 3) data associated with air and ship assets, including trajectories and R/V Sally Ride SEAPOL reflectivity. The current list of available products and their temporal availability is provided in Table S.3.3. These layers can be found through the "+ add layers" button at the bottom of overlays. During the field component, CLAVRX cloud and aerosol products were also posted here.

S.3.3.2 CAMP^{2}Ex Data Portal

Questions persist in the scientific literature about the processes that control the genesis and evolution of tropical convection. This is in part due to the interplay of multi scale processes. Dynamic and thermodynamic conditions of the large-scale environment set-up the scene where individual convective clouds are born, live and die. Yet, the fate of tropical convective clouds is often determined by the interplay between the large-scale environment and storm-scale processes, largely controlled by the microphysical properties of the storms. In turn, these microphysical properties are affected by the aerosol particle content of the environment. As the CAMP^{2}Ex field campaign was designed to help untangle the complex multi-scale processes and interactions that lead to convective development, investigators needed a mechanism to put observation of convective systems into a larger scale meteorological context. For example, before investigators can draw conclusions as to the dominant process affecting convection, they need to distinguish "why" convection from "where" and "how". This requires the application of a visualization capability different from what Geoworldview was optimized for.

To support the science goals of CAMP^{2}Ex, JPL modified the existing JPL North Atlantic Hurricane Watch website (https://nahw.jpl.nasa.gov/; Hristova-Veleva et al., 2020) to create a similar CAMP^{2}Ex portal (https://camp2ex.jpl.nasa.gov). These sites integrate numerous multi parameter satellite data sets, model forecast layers, and airborne observations. Included in the CAMP^{2}Ex portal are interactive visualization and on-line analysis tools allowing quick investigation of the storm structure and evolution. This allows investigator's to: 1) interrogate a large number of atmospheric and ocean variables to help better understand the processes associated with tropical convection; 2) evaluate models by comparison with observations, including the comparison of forecast taus with observations; and 3) access information in consistent formats during the mission planning, post-campaign research and analysis stages.

Included on the CAMP^{2}Ex portal are most of the key satellite products used by meteorologists to forecast convection and tropical cyclone activity, as well as support CAMP^{2}Ex aerosol lifecycle investigations. A list of available data is provided in Table S.3.4, including satellite (AHI scatterometer, radar, microwave, sounder), model (GFS, GEOS-5 and ICAP consensus), and aircraft data (track, dropsonde, APR 3 radar, and microwave). Examples of the interface are provided in Figure S.3.3. In this case, a user started with AHI visible imagery and a microwave precipitation product to diagnose intense shallow versus deep convection relative to the P3 and Learjet 35 flight paths. By utilizing ECVMWF 850 hPa winds, and surface scat sat scatterometery winds, the user could observe that the P3 was sampling a line of intense warm convection with occasional deep turrets formed in an area of surface convergence. By examining multiple hours of data and sensors, this convergence line formed by the interaction of the Southwest Monsoon flow with large scale broad outflow boundaries from a developing Mesoscale Convective System (MCS) that later formed into Typhoon Tapah. By using MODIS Aerosol Optical Depth data, this convergence line is shown to delineated highly polluted air masses from Borneo to the south, with cleaner outflow air formed by the MCs's cold pools to the north. The portal also allows for the polling of key P3 datasets including dropsondes (Figure 3.3.3(b)) and the APR3 radar profiles of

Ku, Ka and w band reflectivity showing intense warm precipitation within the line (Figure 3.3.3(b)).

S.3.3.3 Object-oriented analysis

While CAMP^{2}Ex invested heavily in data acquisition, visualization and contextual analysis, ultimately a framework was required to allow for an appropriate comparison of products. Satellite sensors sample at different efficacies and periods, and aircraft observations are highly localized. Models on the other hand, have an ability to provide detailed simulations over wide areas, but given the stochastic nature of convection lack specificity relative to an individual cloud. In order to bridge observations to models, the team is investigating the use of more object oriented analysis. While models cannot generate an appropriate cloud at the given time and place sampled by aircraft, individual cloud objects can be tracked in model environments similar to the clouds and states sampled by the aircraft and satellites.

Collaborators from NASA Langley Research Center (LaRC) have been prototyping an automated cloud-tracking tool that utilizes the special AHI Rapid Scan dataset acquired during CAMP^{2}EX (e.g., Section 5). The high spatiotemporal resolution of AHI makes it an ideal sensor for capturing cloud lifecycle from space. To maximize the cloud population, the team generated cloud segmentations using AHI 0.5-km visible reflectance for daylit areas, capturing cloud initiation and decay at the smallest possible scales (~1-2 km). The tracking procedure leverages a computer vision package that includes Kalman filters for motion prediction, object overlap search, and the Hungarian (or Kuhn-Munkres) matching algorithm for track designation. Finally, a cataloging procedure compiles all AHI radiances available within the tracked cloud boundaries to form individual spectral histories (e.g., Figure 10(c)). Recent integration with the CLAVR-x geostationary satellite retrieval, produced by SSEC of U. Wisconsin, has enabled comparisons with collocated physical properties such as cloud-top height and droplet size. Although the tracking technique currently relies on daytime hours, thousands of cloud histories can be obtained from a single scene measuring only a few degrees in both dimensions. The particular utility of this technique is that we can evaluate where a cloud was in its lifecycle when it was sampled by the research aircraft (e.g., Figure 10(d)).

In parallel to the satellite based object analysis, Colorado State University has been developing a counterpart analysis based on the Tracking and Object-Based Analysis of Clouds algorithm v1.2 (*tobac*; Heikenfeld et al. 2019) and has successfully enhanced *tobac* through performance improvements, the inclusion of vertical tracking (2D to 3D) and the incorporation of periodic boundary conditions. Using *tobac*, specific modeled cloud objects within CAMP^{2}Ex simulations can be tracked through their attributes, including their convective updrafts (Freeman et al., 2022; Leung and van den Heever 2022). By tracking clouds and their attributes, such as their characteristics in the surrounding modeled dynamical, thermodynamic, and aerosol environments, they can be compared throughout their lifetime to satellite and field observations in an "apples to apples" manner. The team continues to analyze results from multiple campaign days that can be compared against concurrent field measurements and regional meteorological factors. Publications on these analyses are expected in the near future.

S.3.3 References:

Alsweiss, S. O., Jelenak Z., and Chang, P. S. (2017): Remote Sensing of Sea Surface Temperature Using AMSR-2 Measurements, *IEEE Journal of Selected Topics in Applied Earth Observations and Remote Sensing*, , 3948-3954, doi: 10.1109/JSTARS.2017.2737470.

Arnold, N., Putman, W., Freitas, S., Takacs, L., and Rabenhorst, S., 2020: Impacts of new atmospheric physics in the updated GEOS FP system (Version 5.25), GMAO Research Brief, https://gmao.gsfc.nasa.gov/researchbriefs/new_atmos_phys_GEOS-FP/new_atmos_phys_GEOS-FP.pdf.

Aumann, H. H., *Chahine, M. T., Gautier; C., Goldberg; M. D., Kalnay; E., McMillin; L. M., Revercomb; H., Rosenkranz, P. W., Smith; W. L., Staelin, D. H., Strow, L. L., Susskind J.,* (2003): AIRS/AMSU/HSB on the Aqua mission: design, science objectives, data products, and processing systems," in *IEEE Transactions on Geoscience and Remote Sensing*, 41,, 253-264, , doi: 10.1109/TGRS.2002.808356.

Bryan, G. H., and J. M. Fritsch, 2002: A benchmark simulation for moist nonhydrostatic numerical models. Mon. Wea. Rev., 130, 2917–2928, https://doi.org/10.1175/1520-0493(2002)130,2917: ABSFMN.2.0.CO;2., 2002.

Cao, C., Xiong, J., Blonski, S., Liu, Q., Uprety, S., Shao, X., Bai, Y., and Weng, F. (2013): Suomi NPP VIIRS sensor data record verification, validation, and long-term performance monitoring, *J. Geophys. Res. Atmos.*, 118, 11,664– 11,678, doi:10.1002/2013JD020418.

Chen, S., Campbell, T.J., Jin, H., Gaberšek, S., Hodur, R.M., Martin, P.,2010: Effect of Two-Way Air–Sea Coupling in High and Low Wind Speed Regimes. Mon. Weather Rev. 138, 3579–3602. https://doi.org/10.1175/2009MWR3119.1.

Collow, A., Lucchesi, R., and Da Silva, A., 2020: File Specification for GEOS Products Sampled Along Aircraft Trajectories. GMAO Office Note No. 18 (Version 1.0), 36 pp, available from http://gmao.gsfc.nasa.gov/pubs/office_notes.

Collow, A.B.M., V. Buchard, P. Colarco, A. M. da Silva, R. Govidaraju, E. P. Nowottnick, R. Ferrare, C. Hostetler, and L. Ziema, 2022: An Evaluation of Biomass Burning Aerosol Mass, Extinction, and Size Distribution in GEOS using Observations from CAMP2Ex, in prep.

Cotton, W. R., Pielke, R. A. Sr., Walko, R. L., Liston, G. E., Tremback, C. J., Jiang, H., McAnelly, R. L., Harrington, J. Y., Nicholls, M. E., Carrio, G. G., and McFadden, 2003: RAMS 2001: Current status and future directions. Meteorology and Atmospheric Physics, 82, 5–29. https://doi.org/10.1007/s00703-001-0584-9

Da, C (2015): Preliminary assessment of the Advanced Himawari Imager (AHI) measurement onboard Himawari-8 geostationary satellite, Remote Sensing Letters, 6:8, 637-646, doi: : 10.1080/2150704X.2015.1066522

Das, S., Colarco, P. R., Oman, L. D., Taha, G., and Torres, O., 2021: The long-term transport and radiative impacts of the 2017 British Columbia pyrocumulonimbus smoke aerosols in the stratosphere, Atmos. Chem. Phys., 21, 12069–12090, https://doi.org/10.5194/acp-21-12069-2021.

Diner, D. J., Braswell, B. H., Davies, R., Gobron, N., Hu, J., Jin, Y., Kahn, R. A., Knyazikhin, Y., Loeb, N., Muller, J.-P., Nolin, A. W., Pinty, B., Schaaf, C. B., Seiz, G., Stroeve, J., (2005): The value of multiangle measurements for retrieving structurally and radiatively consistent properties of clouds, aerosols, and surfaces, Remote Sensing of Environment, 97, 495-518, doi: https://doi.org/10.1016/j.rse.2005.06.006.

Donlon, C., Berruti, B., Buongiorno, A., Ferreira, M.-H., Féménias, P., Frerick, J., Goryl, P., Klein, U., Laur, H., Mavrocordatos, C., Nieke, J., Rebhan, H., Seitz, B., Stroede, J., & Sciarra, R. (2012): The global Monitoring for Environment and Security (GMES) Sentinel-3 mission, Remote Sensing of Environment,120, 37-57, doi: https://doi.org/10.1016/j.rse.2011.07.024.

Freeman, S.W., D.J. Posselt, J.S. Reid and S.C. van den Heever, 2022: Dynamic and Thermodynamic Environmental Modulation of Tropical Deep Convection in the Maritime Continent. In review at J. Atmos. Sci.

Heidinger, A. K., M. J. Foster, A. Walther, and X. Zhao, 2013: The Pathfinder Atmospheres–Extended AVHRR Climate Dataset. Bulletin of the American Meteorological Society, 95, 909-922

Heikenfeld, M., Marinescu, P. J., Christensen, M., Watson-Parris, D., Senf, F., van den Heever, S. C., and Stier, P., (2019): tobac 1.2: towards a flexible framework for tracking and analysis of clouds in diverse datasets, Geosci. Model Dev., 12, 4551–4570, https://doi.org/10.5194/gmd-12-4551-2019, 2019.

Hersbach, H, Bell, B, Berrisford, P, et al., 2020: The ERA5 global reanalysis. *Q J R Meteorol Soc*. 2020; 146: 1999– 2049. https://doi.org/10.1002/qj.3803

Hristova-Veleva et al., 2020: "An Eye on the Storm: Integrating a Wealth of Data for Quickly Advancing the Physical Understanding and Forecasting of Tropical Cyclones", *Bulletin of the American Meteorological Society,* 2020, DOI 10.1175/BAMS-D-19-0020.1; https://journals.ametsoc.org/doi/pdf/10.1175/BAMS-D-19-0020.1

Figa-Saldaña, J., Wilson, J. J. W., Attema, E., Gelsthorpe, R., Drinkwater, M. R., & Stoffelen A., (2002) The advanced scatterometer (ASCAT) on the meteorological operational (MetOp) platform: A follow on for European wind scatterometers, Canadian Journal of Remote Sensing, 28:3, 404-412, DOI: 10.5589/m02-035

Imaoka, K., Kachi, M., Kasahara, M., Ito, N., Nakagawa K., & Oki, T., (2010): Instrument performance and calibration of AMSR-E and AMSR2, *Proc. Int. Conf. Archives Photogrammetry Remote Sens. Spatial Inf. Sci.*, vol. XXXVIII, part 8 13-16.

Kwan, C., Budavari, B., Bovik, A. C., and Marchisio, G., 2017: Blind quality assessment of fused WorldView-3 images by using the combinations of pansharpening and hypersharpening paradigms, IEEE Geosci and Rem. Sense. Lett. 14, 1835-1839, doi: 10.1109/LGRS.2017.2737820

Levy, R. C., Mattoo, S., Munchak, L. A., Remer, L. A., Sayer, A. M., Patadia, F., and Hsu, N. C.(2013): The Collection 6 MODIS aerosol products over land and ocean, Atmos. Meas. Tech., 6, 2989–3034, https://doi.org/10.5194/amt-6-2989-2013

Leung, G, and S.C. van den Heever, 2022: Updraft structure and detrainment in transient versus terminal congestus clouds. Accepted pending revision at J. Atmos. Sci.

Lynch, P., Reid, J. S., Westphal, D. L., Zhang, J., Hogan, T. F., Hyer, E. J., Curtis, C. A., Hegg, D. A., Shi, Y., Campbell, J. R., Rubin, J. I., Sessions, W. R., Turk, F. J., and Walker, A. L., 2016: An 11-year global gridded aerosol optical thickness reanalysis (v1.0) for atmospheric and climate sciences, Geosci. Model Dev., 9, 1489–1522, https://doi.org/10.5194/gmd-9-1489-2016

Martimort, P., Fernandez, V., Kirschner, V., Isola, C., and A. Meygret, A. 2012: "Sentinel-2 MultiSpectral imager (MSI) and calibration/validation," *2012 IEEE International Geoscience and Remote Sensing Symposium*, 2012, pp. 6999-7002, doi: 10.1109/IGARSS.2012.6351960.

Miller, D. J., Zhang, Z., Ackerman, A. S., Platnick, S., and Baum, B. A., 2016: The impact of cloud vertical profile on liquid water path retrieval based on the bispectral method: A theoretical study based on large-eddy simulations of shallow marine boundary layer clouds. J. Geophys. Res. Atmos., 121, 4122-4141, https://doi.org/10.1002/2015JD024322.

Misra, T., Chakraborty,P., Lad, C. S., Gupta, P., Rao, J., Upadhyay, G., Kumar, S. V., Kumar, B. S., Gangele, S., Sinha, S., Tolani, H., Vithani, K. V., Raman, B. S., Rao, C. V. N., Dave, D. B Jyoti R., and Desai, N. M., (2019): SCATSAT-1 Scatterometer:An Improved Successor of OSCAT. *Current Science*, 117, 941-949, doi: 10.18520/cs/v117/i6/941-949

Mukai, S., Sano, I., and Nakata, M. 2021: Improved algorithms for remote sensing-based aerosol retrieval during extreme biomass burning events, *Atmosphere* 12, no. 3: 403. https://doi.org/10.3390/atmos12030403

Nakajima, T.Y., Ishida, H., Nagao, T.M., Hori, M., Letu, H., Higuchi, R., Tamaru, N., Imoto, N., Yamazaki, A., 2019: Theoretical basis of the algorithms and early phase results of the GCOM-C (Shikisai) SGLI cloud products. *Prog Earth Planet Sci*, **6,** 52. https://doi.org/10.1186/s40645-019-0295-9

Pavolonis, M. J., Heidinger, A. K., & Uttal, T. (2005). Daytime Global Cloud Typing from AVHRR and VIIRS: Algorithm Description, Validation, and Comparisons, Journal of Applied Meteorology, 44(6), 804-826. Doi: https://doi.org/10.1175/JAM2236.1

Platnick, S., Meyer, K. G. .King, M. D., Wind, G., Amarasinghe, N., Marchant, B., Thomas, A. G., Zhang, Z., Hubanks, P. A., Holz, R. E., Yang, P., Ridgway, W. L.. and Riedi, J. (2017): "The MODIS Cloud Optical and Microphysical Products: Collection 6 Updates and Examples From Terra and Aqua," in *IEEE Transactions on Geoscience and Remote Sensing*, vol. 55, no. 1, pp. 502-525, Jan. 2017, doi: 10.1109/TGRS.2016.2610522.

Roy, D. P., Wulder, M. A., Loveland, T. R., Woodcock, C. E., Allen, R. G., Anderson, M. C., Helder, D., Irons, J. R., Johnson, D. M., Kennedy, R., Scambos, T. A., Schaaf, C. B., Schott, J. R., Sheng, Y., Vermote, E. F., Belward, A. S., Bindschadler, R., Cohen, W. B., Gao, F., Hipple, J. D., Hostert, P., Huntington, J., Justice, C. O., Kilic, A., Kovalskyy, V., Lee, Z. P.,. Lymburner, L., Masek, J.G., McCorkel, J,, Shuai, Y., Trezza, R., Vogelmann, J., Wynne, R.H., Zhu, Z. (2014): Landsat-8: Science and product vision for terrestrial global change research, Remote Sensing of Environment, 145, 154-172, https://doi.org/10.1016/j.rse.2014.02.001.

Saleeby, S. M., & van den Heever, S. C., 2013: Developments in the CSU-RAMS aerosol model: Emissions, nucleation, regeneration, deposition, and radiation. Journal of Applied Meteorology and Climatology, 52(12), 2601–2622. https://doi.org/10.1175/JAMC-D-12-0312.1

Sampson, C. R., and A. J. Schrader, (2000): The Automated Tropical Cyclone Forecasting System (Version 3.2). Bull. Amer. Meteor. Soc., 81, 1231-1240. Doi: https://doi.org/10.1175/1520-0477(2000)081%3C1231:TATCFS%3E2.3.CO;2

Sessions, W. R., Reid, J. S., Benedetti, A., Colarco, P. R., da Silva, A., Lu, S., Sekiyama, T., Tanaka, T. Y., Baldasano, J. M., Basart, S., Brooks, M. E., Eck, T. F., Iredell, M., Hansen, J. A., Jorba, O. C., Juang, H.-M. H., Lynch, P., Morcrette, J.-J., Moorthi, S., Mulcahy, J., Pradhan, Y., Razinger, M., Sampson, C. B., Wang, J., and Westphal, D. L., 2015: Development towards a global operational aerosol consensus: basic climatological characteristics of the International Cooperative for Aerosol Prediction Multi-Model Ensemble (ICAP-MME), Atmos. Chem. Phys., 15, 335–362, doiL https://doi.org/10.5194/acp-15-335-2015

Skofronick-Jackson, G., Petersen, W. A., Berg, W., Kidd, C., Stocker, E. F., Kirschbaum, D. B., Kakar, R., Braun, S. A., Huffman, G. J., Iguchi, T., Kirstetter, P. E., Kummerow, C., Meneghini, R., Oki, R., Olson, W. S., Takayabu, Y. N., Furukawa, K., & Wilheit, T. (2017). The Global Precipitation Measurement (GPM) Mission for Science and Society, Bulletin of the American Meteorological Society, 98(8), 1679-1695. Doi: https://doi.org/10.1175/BAMS-D-15-00306.1

Sokolowsky, G.A., S.W. Freeman, and S.C. van den Heever, 2022: Sensitivities of maritime Tropical trimodal convection to aerosols and boundary layer static stability. Accepted pending revision at J. Atmos. Sci.

Sun N., and Weng, F., (2008): Evaluation of Special Sensor Microwave Imager/Sounder (SSMIS) environmental data records, *IEEE Transactions on Geoscience and Remote Sensing*, 46, no1006-1016, doi: 10.1109/TGRS.2008.917368.

Werner, F., Wind, G., Zhang, Z., Platnick, S., Di Girolamo, L., Zhao, G., et al. (2016). Marine boundary layer cloud property retrievals from high-resolution ASTER observations: case studies and comparison with Terra MODIS. *Atmospheric Measurement Techniques*, *9*(12), 5869–5894. http://doi.org/10.5194/amt-9-5869-2016

Winker, D. M., Tackett, J. L., Getzewich, B. J., Liu, Z., Vaughan, M. A., and Rogers, R. R. (2013): The global 3-D distribution of tropospheric aerosols as characterized by CALIOP, *Atmos. Chem. Phys.*, **13**, 3345–3361, doi:10.5194/acp-13-3345-2013.

Witschas, B., Lemmerz, C., Geiß, A., Lux, O., Marksteiner, U., Rahm, S., Reitebuch, O., and Weiler, F.(2020): First validation of Aeolus wind observations by airborne Doppler wind lidar measurements, Atmos. Meas. Tech., 13, 2381–2396, https://doi.org/10.5194/amt-13-2381-2020, 2020.

Yamaguchi, Y., Kahle, A. B., Tsu, H., Kawakami T., and Pniel, M., (1998): Overview of Advanced Spaceborne Thermal Emission and Reflection Radiometer (ASTER)," in *IEEE Transactions on Geoscience and Remote Sensing*, 36, no. 4, 1062-1071, doi: 10.1109/36.700991.

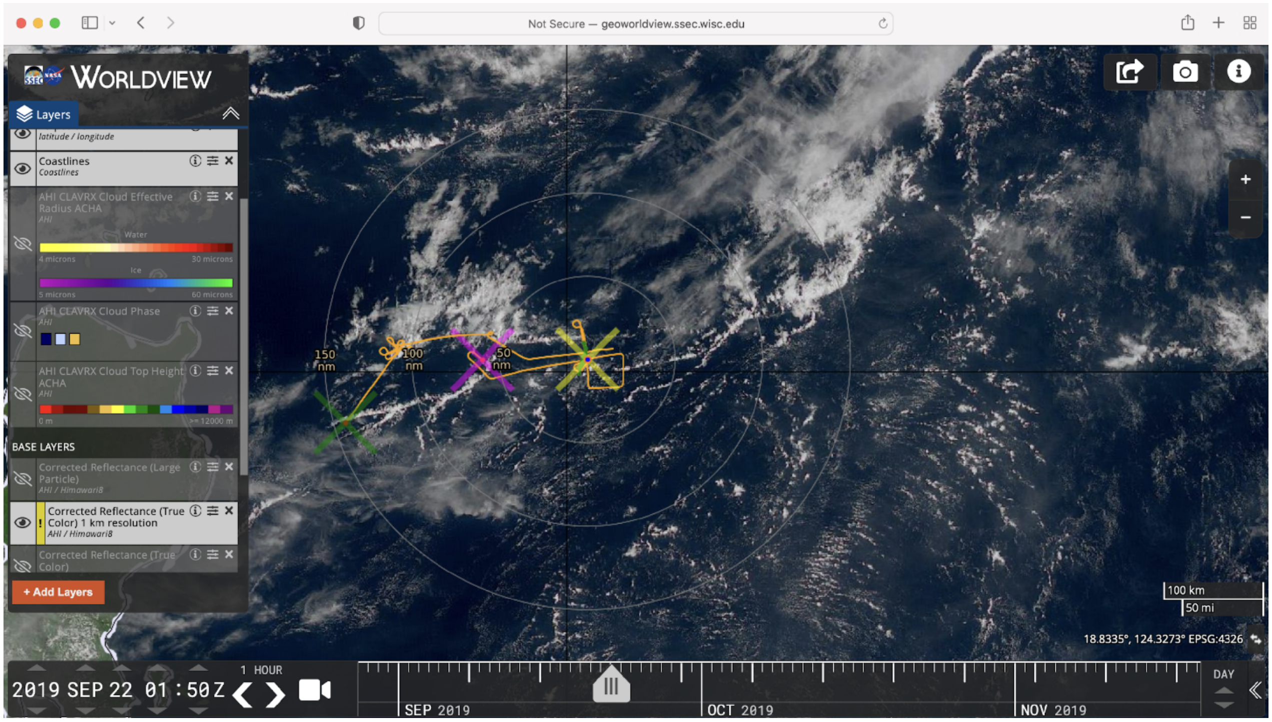

Figure S.3.1 The local instance of the NASA Worldview (https://geoworldview.ssec.wisc.edu) was installed on a server at the hanger in Clark Philippines. It is now hosted at the U. of Wisconsin Space Science and Engineering Center). Custom layers were developed to support the field experiment including the aircraft flight tracks and PISTON ship location shown on this example overlaid on a AHI 1km true color image.

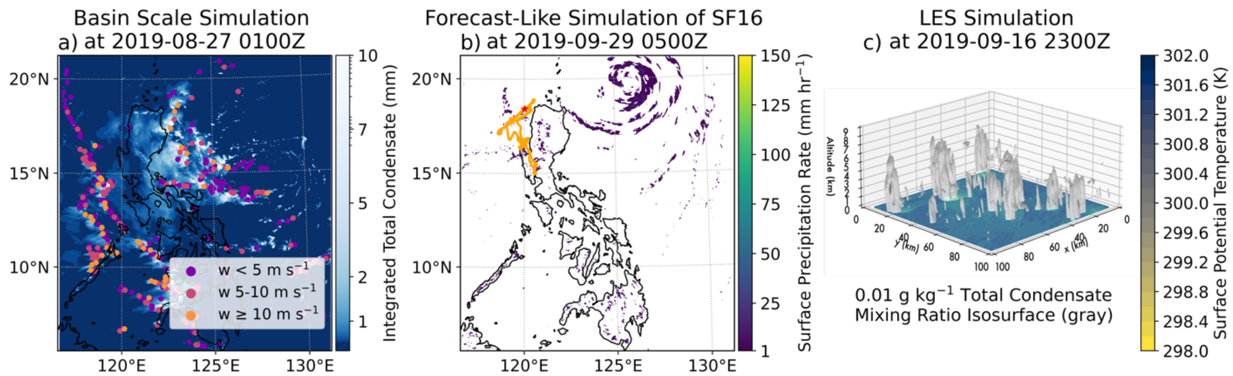

Figure S.3.2: A wide range of RAMS forecasting and research simulations were run in support of the CAMP^{2}Ex field campaign. (a) Integrated total condensate (mm) from one of the basin scale simulations approximately two weeks after initialization (01Z 27 August 2019), showing the wide variety of convective modes captured by these experiments. Overlaid (dots) are locations of identified updraft cores, colored by maximum 3-8 km updraft, that were identified and tracked by the *tobac* algorithm. (b) Snapshot of the Science Flight 16 Forecast-Like simulation at 2019-09-29 0500 Z. Surface precipitation rate (shaded), coastlines (black lines), P-3 flight path (orange line), and location of P-3 at 2019-09-29 0500 Z (red star). Simulations are available for each one of the field campaign days. (c) Snapshot of the LES 23 hours after initialization, showing the presence of shallow cumulus and congestus clouds. Total condensate isosurfaces at 0.01 g/kg shown in gray. Colored surface shows the potential temperature at the lowest model level.

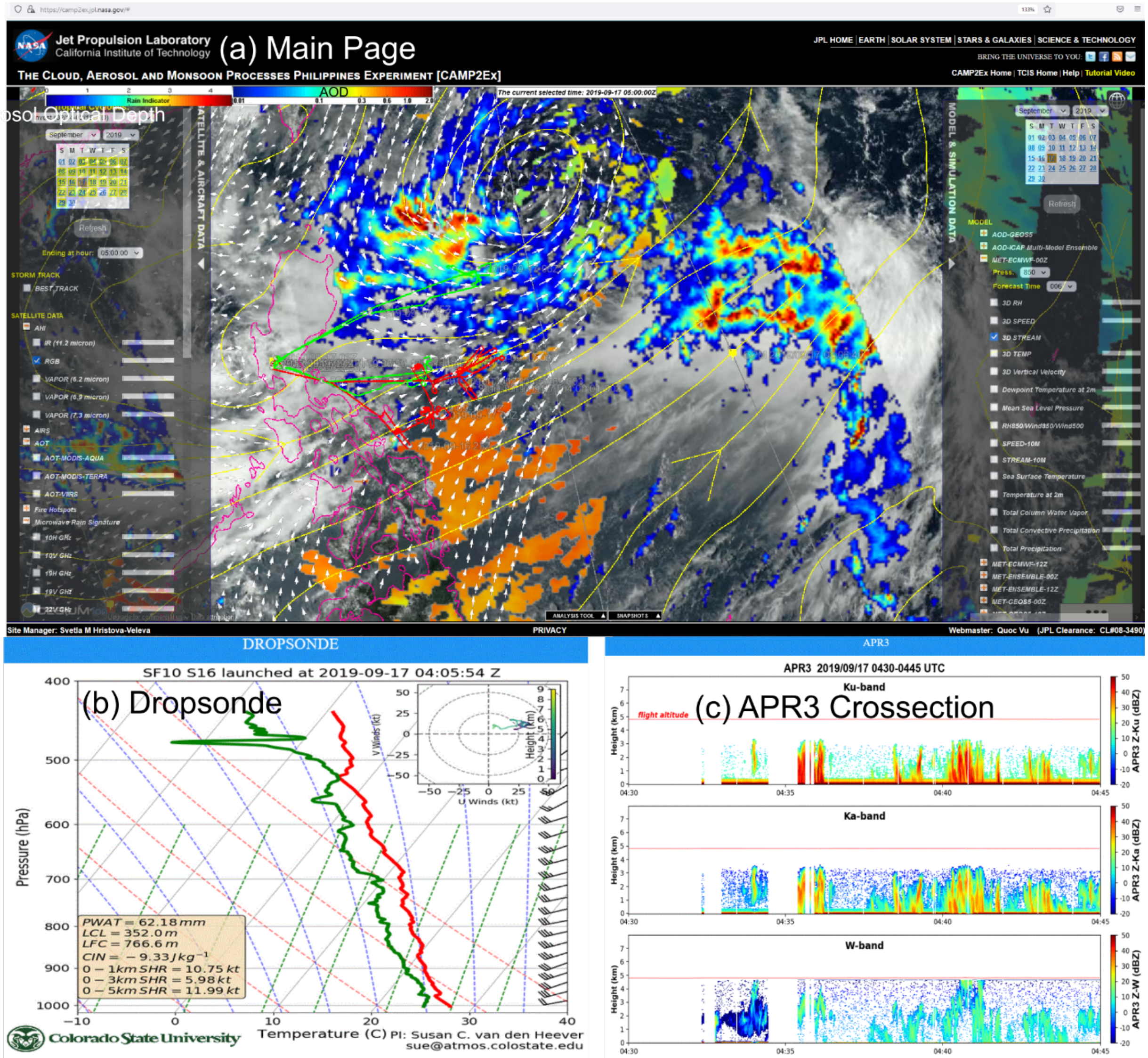

Figure S.3.3 Example display screen components of the JPL data portal for the CAMP^{2}Ex mission for Swept 17, 2019. On this day, the P3 studied convergence line formed from Southwest flow from Borneo bringing high concentrations of smoke, with an outflow boundary from a mesoscale convective system to the north. (a) Main control screen, with P3 (red) and Learjet 35 (green) flight tracks, 850 hPa ECMWF wind streamlines (yellow), Scat Sat surface wind vectors, semi-quantitative microwave precipitation indicator (rainbow), Terra MODIS aerosol optical deoth (green to orange) all on AHI visible imagery. (b) Example P3 dropsonde plot ordered from the main page as the P3 was working an area of convergence. (c) P3's APR3 quicklook ordered form the main page of Ku,. Ka and w band radar as the P3 flew above the convergence line.

Table S.3.1 Satellite remote sensing systems of particular relevance to CAMP2Ex. Sensor: Img=Imager; Vis=Visible; NIR: near IR SW=Shortwave IR; TIR: Thermal IR; Pol=Polarimetery; MW=midwave IR; MicroIm=Microwave Imager; Pol=Polarimeter; Scat=Scatterometer. Orbit: Geo=Geostationary; Inc=Inclined; SunSync=Sun synchronous; Term=Terminator

	Class	**Spacecraft**	**Orbit**	**Products**	**Reference**
Digital Globe, Inc.					
WV110	Img: Vis, NIR	Worldview 2&3	SunSync	Vigh res img, stereo	DigitalGlobe Core Imagery Product Guide
EUMETSAT					
Advanced Scatterometer A&B	Scat.	Metop-A & B	SunSync	Surface wind vectors	Figa-Saldaña et al., 2002
European Space Agency					
Atmospheric Laser Doppler Instrument (ALADIN)	Doppler Wind Lidar	Aeolus	Term.	Wind profiles and aerosol extinction	Witschas et al., 2020
Multispectral Instrument (MSI)	Vis, NIR, SW Img; 10-60 m	Sentinel-2 A&B	SunSync	Imagery, cloud OD & r_{eff}	Martimort et al., 2012
Ocean and Land Colour Instrument (OLCI)	Vis, NIR Img;0.3-1.2 km	Sentinel-3A&B	SunSync	Ocean color products	Donlon et al., 2012
Sea and Land Surface Temperature Radiometer (SLSTR)	Vis, SW, TIR Img; 0.5-1 km	Sentinel-3A&B	SunSync	SST	Donlon et al., 2012
Indian Space Agency					
SCATSAT-1	Scat	PSLV C35	SunSync	Surface winds	Misra et al., 2019
JAXA					

Second generation GLobal Imager (SGLI)	Img: Vis, SW, TIR & Pol.	Global Change Observation Mission Climate (GCOM-C)	Sun Sync	Aerosol and cloud	Mukai et al., 2021 Nakajima et al., , 2019
Advanced Microwave Scanning Radiometer 2 (AMSR-2)	MicroIm	Global Change Observation Mission Water (GCOM-W)	SunSync	Water vapor, Precipitation, SST	Alsweiss et al., 2017 Imaoka et al., 2010
Japan Meteorological Agency (JMA)					
Advanced Himiwari Imager	Img:Vis, NIR, SW, MW, TIR	Himiwari-8	Geo	Imagery, aerosol, cloud & water vapor products	Da (2015)
NASA					
Atmospheric Infrared Sounder (AIRS)	MW-TIR Sounder	Aqua	SunSync	Temperature & water vapor profiles	Aumann et al., 2003
Cloud-Aerosol Lidar with Orthogonal Polarization (CALIOP)	Lidar, 532 &1064 nm	Cloud-Aerosol Lidar and Infrared Pathfinder Satellite Observation (CALIPSO)	SunSync	Attenuated backscatter	Winker et al., 2013
Moderate Resolution Imaging Spectroradiometer (MODIS)	Vis, NIR, SW, MW,TIR Img	Terra& Aqua	SunSync		Levy et al., 2013 Platnick et al., 2017.
Multi Angle SpectroRadiometerr (MISR)	Stereo Img.	Terra	SunSync		Diner et al., 2005

NASA/JAXA					
Advanced Spaceborne Thermal Emission and Reflection Radiometer (ASTER)	Vis-TIR Img, 30-90 m	Terra	SunSync		Yamaguchi et al., 1998
Dual Frequency Precipitation Radar (DPI)	Precip Radar	GPM	Inc-65^{o}	Ka/Ku profiles	Skofronick-Jackson et al., 2017
GPM Microwave Img (GMI)	MicroIm	GPM	Inc-65^{o}		Skofronick-Jackson et al., 2017
NASA NOAA					
Visible Infrared Imaging Radiometer Suite (VIIRS)	Vis, NIR, SW, MW,TIR Img	Soumi NPP. JPSS	SunSync	Imagery, cloud, aerosol properties	Cao et al., 2013
NASA/USGS					
Operational Land Imager	Vis,, NIR, SWIR, TIR Img 15-100m	LANDSAT-8	SunSync	Imagery, cloud T, OD & r_{eff}	Roy et al., 2014
US Dept. of Defense					
Special Sensor Microwave Imager/Sounder (SSMIS)	MicroImg	F15- F18	SunSync	Water vapor, precipitation	Sun and Wang, 2008

Table S.3.2 Operational model data product used in the CAMP^{2}Ex operations and analysis. O=Operational feed; RA=Reanalysis; RE=Research run, AF= Analysis fields; FF Forecast fields

Model	Type	Products	Source
Meteorology			
ECMWF	O	Level DA &Charts	https:// https://www.ecmwf.int/en/forecasts
ERA-5	RA	Level DA	https://cds.climate.copernicus.eu
JMA Surface Charts	O	Charts	https://www-air.larc.nasa.gov/missions/camp2ex/index.html
NAVGEM	O	Level DA	https://usgodae.org
UKMO-Unified Model	O	Charts	https://www-air.larc.nasa.gov/missions/camp2ex/index.html
Composition			
GEOS	O, RA		https://portal.nccs.nasa.gov/datashare/iesa/campaigns/CAMP2EX/
ICAP-MME	O	AOD-A, FF	https://usgodae.org
NAAPS	RA	Level Digital	https://usgodae.org

Table S.3.3. CAMP^{2}Ex Specific Geoworldview (https://geoworldview.ssec.wisc.edu) product availability

	Period	Description
AHI Imagery		
11 um Brightness Temperature	02JUL2018-09JUN2020	10 min, 4 km product
Corrected Reflectance (true color)	02JUL2018-09JUN2020	10 min, 2 km product daylight only (~22-7Z)
Corrected Reflectance (true color)	02JUL2019-31DEC2019	10 min, 1 km product daylight only (~22-7Z)
6.2, 6.9, 7.3 um Brightness Temperature	02JUL2019-31DEC2019	10 min, 4 km high, middle, and low trop water vapor channels
2.2, 3.9 Brightness Temperature		
AHI CLAVR-X Products		
Cloud Top Height	09MAY2019-02DEC2019	10 min, 4 km product
Cloud Phase	09MAY2019-02DEC2019	10 min, 4 km product
Cloud Effective Radius	08AUG2019-02DEC2019	10 min, 4 km product
Assets		
NASA P3 Position	25AUG-05OCT 2019	Location of P3 on the 10 minute, with 30 minute tail
SPEC Learjet 35 Position	25AUG-05OCT 2019	Location of the Learjet on the 10 minute, with 30 minute tail
R/V Sally Ride	15AUG-30SEP2018 5SEP-25SEP, 2019	PISTON Sally Ride Cruise position with 2 hour tail.
SEAPOL Base Reflectivity	5SEP-25SEP, 2019	SEAPOL C Band radar reflectivity from the Sally Ride

1511 Table S.3.4. Available datasets that can be displayed on the JPL CAMP^{2}Ex data portal; https://camp2ex.jpl.nasa.gov/

	Data Products	**Data Source**
Remote sensing Imagery	AHI hourly RGB, IR (11.2 um) & water vapor (6.2, 6.9, 7.3 um)	CIMSS-SSEC
Aerosol Composition	MODIS and VIIRS Aerosol Optical Depth	https://ladsweb.modaps.eosdis.nasa.gov/
Fire	MODIS and VIIRS Active Fire Hotspot	https://ladsweb.modaps.eosdis.nasa.gov/
Microwave rain signatures	GMI, AMSR2, SSMIS microwave brightness temperatures; Rain Index (relative rain rates)	https://arthurhou.pps.eosdis.nasa.gov/
Rain totals (1 hr)	GPM-IMERG	https://arthurhou.pps.eosdis.nasa.gov/
Sea Surface Temperature	MUR-SST	https://podaac.jpl.nasa.gov/
Soundings	AIRS Temperature and Water Vapor Vertical Profiles	https://disc.gsfc.nasa.gov/
Surface Wind (ocean)	ASCAT-A; ASCAT-B; ScatSat SMAP; CYGNSS	https://podaac.jpl.nasa.gov/
Total Precipitable Water	MHS, ATMS (NOAA, MetOp, NPP)	https://disc.gsfc.nasa.gov/
Tropical Cyclone	**Best track:** TC location/max wind/min. MSLP every 6 hours	https://www.ncdc.noaa.gov/ibtracs/
Meteorology Models		
ECMWF	**3D** Temperature/RH/UVW- at standard pressure levels; **2D** 10m winds/2m temperature/2m dewpoint/SST/MSLP/TPW/Total Precipitation/Total Convective Precipitation; RH_{850}/$Wind_{850}$/$Wind_{500}$	ECMWF
GEOS5	**3D** Temperature/RH/UVW at standard pressure levels; **2D** 10m winds/2m temperature /surface temperature/ TPW/Ice & Liquid Water Path; RH_{850}/$Wind_{850}$/$Wind_{500}$	NCCS/GSFC MDISC
GFS	**3D** Temperature/RH/UVW - at standard pressure levels; **2D** 10m winds/surface temperature/MSLP/TPW RH_{850}/$Wind_{850}$/$Wind_{500}$	https://nomads.ncep.noaa.gov/
Composition Models		

GEOS-5	**2D** AOD – Total, coarse & fine; Surface particulate matter	https://www.nccs.nasa.gov/
ICAP-MME	**2D** AOD – Total, coarse, & fine multi model consensus	https://usgodae.org/
Platform Data		
Tracks	NASA P-3; SPEC Learjet 35; *R/V Sally Ride*	https://www-air.larc.nasa.gov/missions/camp2ex/
Instrument Quick Looks	APR-3 reflectivity; AMPR brightness temperatures; AMPR ocean surface winds; Skew-Ts from the dropsondes	https://www-air.larc.nasa.gov/missions/camp2ex/

Supplemental S.4 Acknowledgements

The NASA CAMP^{2}Ex Mission was conceived and conducted by a large community of researchers and programmatic partners. Funding and programmatic direction was provided by the NASA Radiation Sciences Program and Airborne Science Program, with supplemental flight hour, ground site, science, and management support by the US Naval Research Laboratory Base Program and the sponsors of the Manila Observatory. The planning, deployment and post mission analysis required the cooperation of numerous research entities and individuals, with only a fractional few as coauthors of this paper. Especially notable contributions include the following:

We would like to thank the many Philippine government entities for their cooperation in mission operations including PAGASA, the Department of Foreign Affairs (DFA), Philippine Department of Science and Technology (DOST), Civil Aviation Authorities of the Philippines (CAAP), and Armed Forces of the Philippines (AFP). We are likewise grateful to the U.S. Embassy in Manila Economics and Science Department for shepherding the mission over many years of preparation, especially Maria Theresa “Bimbi” Villa, Claire T. Bea, Alma Green, and Nicole P. Fox. We are also grateful for other staff that supported the mission and left the embassy long before it could be executed, starting with Caron de Mars, and Dovas Saulys as well as many at the Defense Attaché Office. We are also appreciative for the international program support provided by the NASA Office of International and Interagency Relations, and in particular Mrs. Judy Dove.

CAMP^{2}Ex was conceived jointly with the Ateneo de Manila University and Manila Observatory and we would like to thank them for their partnership. In particular we would like to thank Ms. Antonia (Toni) Yulo- Loyzaga and Fr. Daniel J. McNamera, S.J. for logistical and science guidance. We are also grateful to Fr Jose Ramon “‘Jett” T. Villarin, S. J. and Dr. Evangeline T. Bautista for support from Ateneo de Manila University.

Logistical support for the CAMP^{2}Ex mission was provided by the substantial efforts of the Earth Science Project office, with special thanks for Sommer Nicholas, Quincy Allison, and Brent Williams for their outstanding efforts with the mission shipping and logistics. Also, to Susan McFadden, Katie Stern, Alex Stanfill, Vidal Salazar, Marilyn Vasquez, Bernie Luna, Erin Czech, Dan Chirica, and Lynn Kennedy for their support with the mission coordination, management, and IT infrastructure. NASA P3 aircraft integration and management was provided by the NASA Wallops Flight Facility (WFF). We wish to thank the facility’s staff and the substantial support of many engineers, we are particularly grateful to Kelly Griffin for her help to interface the science team (WFF). Additional information technology support was provided by Erica Stith, David Van Gilst and Melissa Yang of NASA's National Suborbital Research Center (NSRC) and by Dr. Aaron Duley and his team for their invaluable support integrating CAMP^{2}Ex into the Airborne Science Program Mission Tool Suite. The integration of aircraft data, satellite data, and real time air-ground communication were critical to the safe and successful execution of the CAMP^{2}Ex flights. Mission success was dependent the outstanding cadre of pilots for the NASA P3 including CAPT James Lawson, USN and CAPT Rodney Turbak, USN as pilots in command, and Alan Barringer, John Baycura, Brian Bernth, LT Brandin Merrirr, USN, to which the team is most indebted. Indeed, the flying environment was quite complex, with rapidly shifting airfield, air traffic, and convection conditions. We are also grateful for their input for coordination with Philippine aviation authorities and flight planning scientists.

The several organizations at Clark that made our operations possible, including Piero Rodriguez, Peter Rodriguez, Peter A. Rodriguez Jr., Edilberto Medina, and Arnold Santiago from Asian Aerospace; Jaime Alberto Melo from the Clark Airport International Corporation (CIAC); Bi Yong Chungunco and Paolo Santos from Luzon International Premier Airport Development (LIPAD). Outstanding logistical support and coordination was also provided by Mr. Bob Gillis, Mrs. Gloria Gillis, and Ms. Zoe Gillis; from South Pac Diversified Services (SPDS Inc.) in Subic Bay, as well as Mr. Karim Israel from Clark Airport Support Services.

CAMP^{2}Ex was conducted during the Years of the Maritime Continent, and for the contributions of that cooperative effort we would like to thank Kunio Yoneyama (JAMSTEC), Chidong Zhang (NOAA PMEL), and Olivia Cabrera (University of the Philippines).

Early morning (1 am PHT) forecasts to aide in the "go/no go" decision on flight days were provided by students and postdocs at the University of Illinois at Urbana-Champaign, including Yulan Hong, Puja Roy, Arka Mitra, and Piyush Garg. In addition, Guangyu Zhao, Yizhe Zhan, Jesse Loveridge, and Piyush Garg provided quick turn-around analyses of satellite and flight-track data for post-flight science debriefs. The University of Illinois team would also like to thank Greg McFarquhar from the University of Oklahoma for his tremendous help in interpreting several of the CAMP^{2}Ex datasets and early analyses.

Forecast support for flight planning was provided by NASA's Global Modeling and Assimilation Office (GMAO) in the form of custom imagery posted on their Framework for Live User-Invoked Data (FLUID) webpage. We would like to thank Joe Ardizzone, Brent Smith, Christine Bloecker, and Karla Longo for conceptualizing and configuring the imagery.

The JPL CAMP^{2}Ex data portal (https://camp2ex.jpl.nasa.gov) integrates model forecasts with multi-parameter satellite and airborne observations from a variety of instruments. It was developed to support the goals of the campaign, serving as a rich information source during the mission planning and post-campaign research and analysis stages, helping scientists gain intuition in the complex meteorological and aerosol environment posed by the southwest monsoon. We would like to thank P. Peggy Li, Brian Knosp, Quoc Vu, and F. Joseph Turk for their dedication to the development of this portal system, for their close attention during the operational phase of the campaign to make sure that the system operated flawlessly, and to their continued efforts in operating the portal system since the summer of 2018 and until present, providing extended period of observations in the CAMP2Ex domain with the goal to support analyses of the interannual variability in the region.

Meteorological support for operations is gratefully acknowledged by the Japan Meteorological Agency for expedited AHI acquisition, processing, delivery; the Joint Typhoon Warning Center for TC forecasting; and PAGASA for airfield forecasting and regional radar. Geostationary and polar sensor science processing, distribution and visualization was performed with the special help of the University of Wisconsin-Madison Space Science and Engineering Center (SSEC) and its Science Investigator-led Processing Systems (SIPS). We gratefully acknowledge the special help from Willem Marais and Coda Philips at SSEC for implementing the near real time processing within both AWS and locally at SSEC during the experiment. We are likewise appreciative for special remote sensing orders by ESA for Sentinel 2, and by Ann Marie Wytzka (NRL DC) for DigitalGlobe worldview collections.

The AMPR team gratefully acknowledges the scientists and engineers who supported AMPR during its deployment, assisted with data system debugging early in the campaign, and provided feedback during post-mission data analyses. Special thanks are given to Doug Huie for providing engineering support in the field. Thanks are also owed to: Paul Meyer, Eric Cantrell, Sayak

Biswas, Kurt Dietz, Mark James, Carl Benson, Karthik Srinivasan, Sue O'Brien, Dave Simmons, and Max Vankeuren. Financial support for AMPR was provided by NASA Headquarters, and Corey Amiot acknowledges funding support from NASA Marshall Space Flight Center (MSFC) through Cooperative Agreement NNM11AA01A between NASA MSFC and The University of Alabama in Huntsville.

CAMP^{2}Ex's public and student outreach involved over 1,500 students and 100 teachers at thirty nine different schools. The effort was managed by Dr. Emily Shaller from the Bay Area Environmental Research Institute (BAER), the Manila Observatory, and it benefited from the support of local schools as well as the Global Learning and Observation to Benefit the Environment (GLOBE) Philippines program. CAMP^{2}Ex personnel, including scientists, pilots, program and project managers, all contributed to making the outreach a success.

With the delay of the original CAMP^{2}Ex mission by one year, a second PISTON research cruise (following a successful 2018 campaign) in collaboration with CAMP^{2}Ex was funded by the Office of Naval Research and organized by the PISTON Science Team. In 2018, PISTON was jointly funded by the Office of Naval Research and the NOAA Climate Program Office's Program on Climate Variability and Predictability. PISTON instrumentation and real-time modeling support aided the 2019 CAMP^{2}EX campaign. We acknowledge the support and flexibility of officers and crew of the Research Vessel *Sally Ride* of Scripps Institution of Oceanography. In particular we would like to thank Simon de Szoeke (Oregon State), Harindra Joseph Fernando and Jay Orson Hyde (Notre Dame), as well as Sergio Pezoa, Byron Blomquist, Ludovic Bariteau (NOAA PSL), led by Christopher Fairall and Elizabeth Thompson (NOAA PSL) for the effort required to make the much needed near surface ocean, atmosphere, and flux measurements, and the Colorado State team that supported the SEAPOL radar and radiosonde regiment, including Kyle Chudler and Brenda Dolan, led by Steven A. Rutledge. Ocean measurements were supported by Pavan Vutuku, Kerry Latham, and Kenneth Hughes from Oregon State University, led by James N. Moum.